



Investigating the role of aerosol wet scavenging on global horizontal irradiance simulation in the WRF-Chem-solar model

Su Wang^a, Gang Huang^{b,c,*}, Tie Dai^{b,d,**}, Junji Cao^e, Letu Husi^f, Run Ma^g, Cuina Li^h

^a State Key Laboratory of Numerical Modeling for Atmospheric Sciences and Geophysical Fluid Dynamics, Institute of Atmospheric Physics, Chinese Academy of Sciences, Beijing 100029, China

^b State Key Laboratory of Earth System Numerical Modeling and Application, Institute of Atmospheric Physics, Chinese Academy of Sciences, Beijing 100029, China

^c University of Chinese Academy of Sciences, Beijing 100049, China

^d Collaborative Innovation Center on Forecast and Evaluation of Meteorological Disasters (CIC-FEMD), Nanjing University of Information Science and Technology, Nanjing 210044, China

^e Institute of Atmospheric Physics, Chinese Academy of Sciences, Beijing 100029, China

^f State Key Laboratory of Remote Sensing Science, Aerospace Information Research Institute, Chinese Academy of Sciences, Beijing 100081, China

^g Artificial Intelligence Key Laboratory of Sichuan Province, Sichuan University of Science & Engineering, Yibin 644005, China

^h Meteorological Observation Center of China Meteorological Administration, Beijing 100081, China

HIGHLIGHTS

- A physical based parametric aerosol wet scavenging scheme has been implemented in the WRF-Chem-Solar model.
- The updated scheme improves AOD simulation, reducing BIAS by 20%, with notable enhancements in Central & Eastern China.
- The new scheme significantly amends the positive bias of the GHI by 36.47%/29.91% under clear and all sky conditions in China.

ARTICLE INFO

Keywords:

Aerosol wet scavenging
Global horizontal irradiance
WRF-Chem-solar
Model simulation

ABSTRACT

Solar energy emerges as a vital renewable resource with profound implications for future energy consumption. To improve the accuracy of global horizontal irradiance (GHI) simulation, this study integrates the Thompson and Eidhammer aerosol-aware cloud microphysics scheme with the aerosol module Goddard Ozone Chemistry Aerosol Radiation and Transport (GOCART) in the WRF-Solar model. Based on the new coupled aerosol-cloud interaction, a physical parametric aerosol wet scavenging scheme is developed to investigate its effects on aerosol and GHI simulations. Our results demonstrate that the updated wet removal enhances the spatial representation of aerosol optical depth (AOD) across China, particularly in regions influenced by anthropogenic aerosols such as Northern, Central and Eastern China. The average absolute mean bias (BIAS) value for AOD decreases by 20.00%, leading to a 36.47% improvement in reducing the overestimation of GHI under clear sky. The most remarkable BIAS reductions occur in Central (104.30%), Western (45.70%), and Eastern China (41.42%) for GHI under clear sky, especially in high surface solar radiation zones ($>500 \text{ W/m}^2$). Similar improvements are observed for GHI under all-sky conditions, with a national relative improvement of 29.91%. Central, Eastern, and Western China show the most substantial BIAS reductions, with relative decreases of 57.48%, 50.62%, and 32.40%, respectively. Overall, this study highlights the potential of the enhanced aerosol wet scavenging scheme to improve GHI simulation accuracy, providing valuable insights for advancing renewable energy initiatives.

1. Introduction

Solar energy, as a green and renewable energy resource, has

experienced rapid growth during global energy transitions [1], particularly in China. Under China's 2060 carbon neutrality goal, the rapid deployment of photovoltaic systems has created an urgent demand for

* Corresponding author.

** Corresponding author.

E-mail addresses: hg@mail.iap.ac.cn (G. Huang), daitie@mail.iap.ac.cn (T. Dai).

<https://doi.org/10.1016/j.apenergy.2025.126062>

Received 4 December 2024; Received in revised form 2 April 2025; Accepted 4 May 2025

Available online 5 June 2025

0306-2619/© 2025 Elsevier Ltd. All rights reserved, including those for text and data mining, AI training, and similar technologies.

precise surface solar radiation prediction [2]. The global horizontal irradiance (GHI) is the first and one of the most essential variables in most solar radiation prediction and simulation systems [3]. While GHI under clear-sky conditions is known for its abundant solar resources, GHI forecasting and simulating under all-sky conditions remains a significant challenge [3,4]. Physically-based numerical weather prediction (NWP) models are considered the primary method for GHI prediction and simulation over temporal and spatial scales exceeding 6 h [5]. However, their accuracy is constrained by the performance of the simulated aerosol-cloud-radiation processes [6,7].

By perturbing the cloud properties and radiation budget, aerosols play a significant role in Earth's energy balance via aerosol-radiation and aerosol-cloud interactions (ARIs/ACIs) [8]. Earlier studies reveal that online ARIs/ACIs have superiority in describing the aerosol-cloud-radiation process [9–11]. However, they are only considered in NWP models that explicitly resolve atmospheric chemistry, which increases computational costs and are limited use in the GHI simulation [12].

Furthermore, significant uncertainties remain in the aerosol wet scavenging process among regional and global models, which substantially impact the GHI simulation [13,14]. Aerosol wet scavenging, including in-cloud and below-cloud removal processes, is the primary removal pathway for aerosols. It is typically described as prescribed aerosol scavenging ratios to minimize computational burden [13,15,16]. However, wet scavenging is highly sensitive to variations in chemical species and meteorological conditions, further limiting their simulation accuracy [17].

To address these challenges, the Weather Research and Forecasting model with solar extensions (WRF-Solar) has been specifically developed [6]. Its Thompson and Eidhammer aerosol-aware microphysics scheme (hereafter referred to as TE14) [18] balances computational cost and system complexity and effectively represents aerosol-cloud-radiation processes [19]. With aerosol information from a multi-year (2001–2007) simulation of the Goddard Chemistry Aerosol Radiation and Transport (GOCART) model [20] or outputs from other chemistry models, WRF-Solar incorporates indirect aerosol effects, aerosol dispersion, transport, and cloud microphysics interactions [21].

Several studies have evaluated the benefits of using the TE14 scheme to improve GHI forecasting and simulation accuracy [4,6,22–24]. Jimenez et al. [6] found a 23 % relative improvement for GHI compared to the official WRF-Solar version which lacks aerosol representation under clear sky. Aerosol Optical Depth (AOD) is a critical parameter for assessing aerosol optical properties, representing the degree to which aerosols attenuate light transmission through scattering or absorption [25]. Saide et al. [26] compared this setup with a more complex aerosol-cloud-radiation scheme and found similarities in AOD and aerosol impacts on near-storm environments. Weston et al. [24] revealed a better representation of realistic values for number concentration, liquid water content, mean volumetric diameter, and droplet size distribution in Namibia compared to the original version. Jimenez et al. [23] assessed its performance on GHI simulation and found a strong spatial correlation (over 0.90) with values derived from satellite-derived irradiance.

Other studies have attempted to improve the model's performance. One study firstly coupled the GOCART aerosol mode online with the Goddard [27] and the Rapid Radiative Transfer Model for Global Circulation Models (RRTMG) [28] shortwave radiation schemes in WRF-Solar, focusing on aerosol-induced direct effects on GHI [29]. However, it lacks considering the aerosol indirect effects, as the GOCART model only generates mass concentration without number concentrations, the latter are necessary for the microphysics scheme. Another study investigated the real-time indirect effects of dust aerosol by coupling dust from the GOCART aerosol model and TE14 microphysics scheme in WRF-Chem version 3.8.1 [30], but the other aerosol categories' information is still derived from climatological data mentioned above.

In summary, some limitations still persist. Firstly, the climatological aerosol emission data cannot accurately represent the realistic changing aerosol level, particularly in highly polluted regions such as North

China. Previous studies have demonstrated that unrealistic assumptions of aerosol will lead to large biases of AOD [31], which is the main source of GHI error under clear-sky conditions [32]. Secondly, even with aerosol information from GOCART, the scheme lacks a physical-explicit representation of wet scavenging. Instead, the default wet scavenging coefficients of each species are constant values. Therefore, more modifications are required for a fully coupled simulation.

This study aims to fully couple the TE14 microphysics scheme with the GOCART model, integrating the online aerosol-cloud-radiation interactions into the WRF-Solar model (hereafter referred to as WRF-Chem-Solar). Furthermore, a physically-based parametric aerosol wet scavenging scheme is implemented to further improve its performance. This study will contribute to advancing our understanding of the updated aerosol-related process and its impact on GHI simulation.

The remainder of the paper is presented as follows. Section 2 describes the model configuration. Section 3 describes the implementation work for coupling the TE14 scheme and the GOCART aerosol model in WRF-Solar. Section 4 presents the experimental designs, as well as satellite and observation datasets used to validate the performance of the model. Section 5 presents the results, followed by the conclusions and discussions in Section 6.

2. Model description

In this study, Weather Research and Forecasting model coupled with Chemistry (WRF-Chem) model version 4.4 is applied [33]. Developed by the National Center for Atmospheric Research (NCAR), WRF-Chem is an online-coupled mesoscale numerical weather prediction system designed to simulate and forecast atmospheric chemical and physical processes at regional scales. Further details are provided in the supplementary information. In comparison to the earlier version, which only includes water/ice-friendly aerosol in the TE14 scheme, version 4.4 incorporates a black carbon aerosol category as well as its radiative effect [33,34]. WRF-Solar is a specialized configuration and augmentation of the WRF model [6]. It blends the advantages of the Multi-Sensor Advection Diffusion Nowcast (MADCast) [35,36] and implements feedback between sub-grid scale clouds and shortwave irradiance through a shallow cumulus parameterization [37]. In the frame of the original WRF-Solar model, it is not coupled online with the chemistry aerosol module. Even when the chemistry module is activated, discrepancies in calculation units between the chemistry and microphysics modules prevent the seamless integration of aerosol information into cloud microphysics, let alone the updating wet scavenging of aerosols.

This study focuses on the bulk GOCART aerosol model to reduce computational costs [38]. The model simulates the mass mixing ratios of major tropospheric aerosol components, including sulfate, hydrophobic and hydrophilic organic carbon and black carbon (OC1, OC2, BC1, and BC2), size-resolved mineral dust and sea salt. These aerosols, which serve as dominant cloud condensation nuclei (CCN) and ice condensation nuclei (IN), play a critical role in cloud processes globally [18].

To relieve the high computational burden and complexity, the TE14 microphysics scheme simply classifies the aerosols into three types: hygroscopic aerosols as “water friendly” aerosols (NWFA), non-hygroscopic aerosols as “ice friendly” aerosols (NIFA) and black carbon (BC). It specifies the activation of aerosols serving as CCN and IN. Then it explicitly predicts the number concentrations of cloud droplets and ice crystals by assuming log-normal distributions with characteristic diameters and geometric standard deviations [39]. The nucleation of dust particles into ice crystals, as described by DeMott et al. [40] is employed. By providing a surrogate surface emission and interpolating the climatology aerosol fields to the WRF grid pressure levels, the number concentrations of aerosols will be updated at each time step based on changing meteorological field (such as the wind vector, fall speed and interaction with cloud), the concentrations of cloud droplets, snow, and graupel are predicted, and the indirect effects of aerosols are evaluated [18].

Generally, the WRF-Chem model relies on a simplified parametric wet scavenging scheme with fixed ratios: 0.5 for BC₁, OC₁, dust and dimethylsulphide (DMS), 0.8 for BC₂ and OC₂, 1 for sea salt and sulfate, which proved to result in excessively strong aerosol wet removal in earlier studies [41,42]. For example, the ratio for coarse insoluble dust is set to 0.4 in the ECHAM5-HAM model, significantly lower than those used in existing WRF-Chem configurations [43]. Therefore, a more explicit physically-based parametric wet scavenging scheme should be developed.

3. Implementation of GOCART–Thompson microphysics scheme

Since the GOCART model does not predict the aerosol number concentrations required in the TE14 microphysics scheme, a significant challenge in coupling the TE14 scheme with the GOCART model lies in converting aerosol mass concentrations into number concentrations of NWFA, NIFA and BC used in the TE14 scheme, the overall pattern diagram is shown in Fig. 1.

A lookup table is developed to predict the number concentrations of each aerosol. Firstly, the microphysical properties of all the species used for the mass-to-number conversion are required, as listed in Table 1. These properties include particle density, modal and effective radius, the geometric standard deviation of the lognormal size distribution, and the upper and lower limits of the particle sizes. All values are derived from the Optical Properties of Aerosols and Clouds (OPAC) dataset [44]. In the GOCART model, the actual number of aerosol species involved in the chemical calculation is fourteen. Specifically, for sea salt, four size bins with radius of 0.1 μm–0.5 μm, 0.5 μm–1.5 μm, 1.5 μm–5 μm, and 5 μm–10 μm are included (SEA1–4). For dust particles, the radius ranges from 0.1 μm to 10 μm: 0.1 μm–1 μm, 1 μm–1.8 μm, 1.8 μm–3 μm, 3 μm–6 μm, and 6 μm–10 μm (DUST1–5). The DUST1 range from 0.1 to 1 μm is further divided into four size bins: 0.1 μm–0.18 μm, 0.18 μm–0.3 μm, 0.3 μm–0.6 μm, and 0.6 μm–1 μm in the related code when calculation [45]. All sea salt at coarse mode (SEA 2–4) is aggregated, as is the case for BC₁ and BC₂.

We assume lognormal size distributions with characteristic diameters and geometric standard deviations, as described in Chin et al. [39] for the number density calculation of aerosol components, the equation can be described as follows [44,46]:

$$\frac{dN_i(r)}{dr} = \frac{N_i}{\sqrt{2\pi r \log \sigma_i \ln 10}} \exp\left(0.5 \left(\frac{\log \frac{r}{r_{modN_i}}}{\log \sigma_i}\right)^2\right) \quad (1)$$

where r_{modN_i} represents the mode radius, σ_i measures the width of the distribution, N_i means the total particle number density of each component i in particles per size bin, and r is the particle radius per size bin.

Then all components have been assumed to be spherical to calculate their mass contribution per particle by the following equation:

$$q_{unit} = \frac{4}{3} \pi r^3 \rho \quad (2)$$

where q_{unit} represents mass per unit particle for a size bin r , ρ is the density of the aerosol particles.

Subsequently, the number concentration per size bin is calculated by N_i times q_{unit} . After summing up the number concentrations across all size bins, the total number concentration for each species is calculated by:

$$N_{tot_i} = \sum N_i q_{unit} \quad (3)$$

where N_{tot_i} means the total number concentrations for each species through all size bins per unit mass. Then a candidate look-up table is created to transform the mass concentrations into number concentrations per unit mass, as shown in Table 1.

With the online-calculated mass concentration of aerosol species from the GOCART model, we can calculate the final number concentrations (Nt) through multiplying the mass concentrations by the number concentration per unit mass ($Ntot$) for each time step of the fourteen types.

Specifically, in the TE14 scheme, NWFA is calculated by combining sulfate, OC₁, OC₂, and SEA1–4, which are considered the source of CCN. NIFA is calculated by accumulating dust particles larger than 0.5 μm (diameter), which are seen as the source of IN. Therefore, only dust particles diameter larger than 0.5 μm (for dust size in 0.18 μm–0.3 μm, only modal radius larger than 0.25 μm is calculated) contribute to NIFA. This approach differs from earlier work [30], which summed up all the dust as NIFA. Afterward, the time-varying number concentrations of

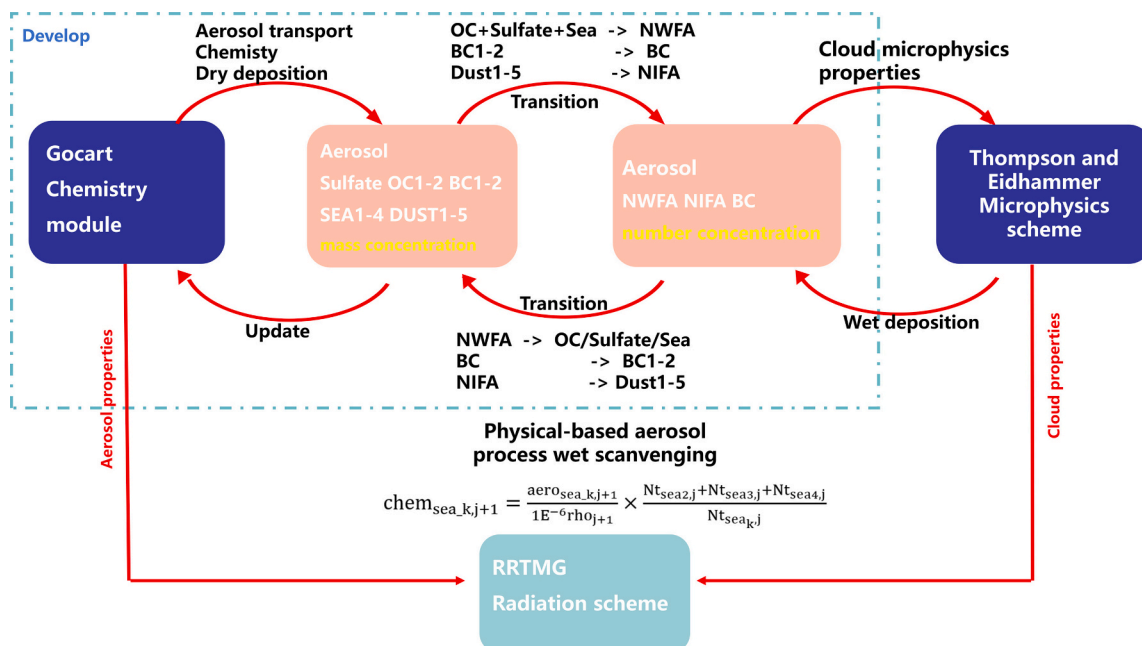


Fig. 1. The pattern diagram of the WRF-Chem-Solar model we develop.

Table 1
Microphysical properties of aerosol components in dry state [44] and its number concentration per unit mass (N_{tot}).

Aerosol type	Standard deviation	Mode radius [micron]	Minimum radius [micron]	Maximum radius [micron]	Density [g/cm^3]	N_{tot} [#/ g]
Sulfate	2.03	0.0695	0.005	20.00	1.70	5.85E+13
OC ₁	2.51	0.4710	0.005	20.00	2.00	1.49E+16
OC ₂	2.24	0.0212	0.005	20.00	1.80	3.77E+12
BC ₁ + BC ₂	2.00	0.0118	0.005	20.00	1.00	7.69E+14
SEA1	2.03	0.2090	0.005	20.00	2.20	4.96E+12
SEA2-4	2.03	1.7500	0.005	60.00	2.20	3.20E+09
DUST1_1	1.95	0.0421	0.005	20.00	2.60	0.0
DUST1_2	1.95	0.0722	0.005	20.00	2.60	4.54E+12
DUST1_3	1.95	0.1354	0.005	20.00	2.60	1.36E+12
DUST1_4	2.00	0.2407	0.005	20.00	2.60	2.09E+11
DUST2	2.00	0.4212	0.005	20.00	2.60	4.13E+10
DUST3	2.00	0.7220	0.005	20.00	2.60	7.76E+9
DUST4	2.15	1.3540	0.005	60.00	2.60	1.26E+9
DUST5	2.15	2.4070	0.005	60.00	2.60	2.04E+08

NWFA, NIFA, and BC are obtained by summing up all the related aerosol numbers and then passed into the TE14 microphysics scheme. Subsequently, they will be translated into CCN and IN using a look-up table of activated fraction determined by the model's predicted temperature, vertical velocity, number of available aerosols, predetermined values of hygroscopicity parameter and aerosol mean radius [18].

During each time step of the cloud microphysical processes calculation, the number concentrations of NWFA, NIFA, and BC are updated, and the online aerosol-cloud interaction is activated. Then a physically-based wet scavenging scheme is activated to calculate the aerosol loss related to microphysical processes. Descriptions of the process rate terms for NWFA and NIFA can be found in Eqs. (4–5) below. Further detail on the governing conservation equation can be found in [18].

$$\frac{dN_{wfa}}{dt} = - \left(\begin{array}{c} \text{rain, snow, graupel} \\ \text{collecting aerosols} \end{array} \right) - \left(\begin{array}{c} \text{homogeneous nucleated} \\ \text{deliquesced aerosols} \end{array} \right) - \left(\begin{array}{c} \text{CCN} \\ \text{activation} \end{array} \right) + \left(\begin{array}{c} \text{cloud and rain} \\ \text{evaporation} \end{array} \right) + \left(\begin{array}{c} \text{surface} \\ \text{emissions} \end{array} \right) \quad (4)$$

$$\frac{dN_{ifa}}{dt} = \left(\begin{array}{c} \text{rain, snow, graupel} \\ \text{collecting aerosols} \end{array} \right) - \left(\begin{array}{c} \text{IN} \\ \text{activation} \end{array} \right) + \left(\begin{array}{c} \text{cloud ice} \\ \text{sublimation} \end{array} \right) + \left(\begin{array}{c} \text{surface} \\ \text{emissions} \end{array} \right) \quad (5)$$

where N_{wfa} and N_{ifa} represent the aerosol number concentration. In Eqs. (4), the first term on the right-hand side represents the removal of aerosols by precipitation scavenging. The second term means the homogeneous nucleation of deliquesced aerosols which is returned to N_{wfa} . The third term represents the loss of aerosols due to activation as CCN. The fourth term shows aerosols gain due to the evaporation of cloud droplets and raindrops. The fifth shows aerosol from surface emissions. The content of Eqs. (5) is similar and will not be repeated here.

As mentioned earlier, wet deposition is highly sensitive to the chemical species retained during cloud drop freezing. However, even when coupling the GOCART model with the TE14 scheme, the removal of aerosol information is not updated in the GOCART model because these changes are not directly considered in the TE14 (which calculates only NWFA, NIFA, and BC), leading to mismatches between the two processes. In the default WRF-Chem version, it uses a simplified resolved wet scavenging scheme ($wetscav_onoff = -1$). Actually, the wet scavenging coefficients of aerosols vary with time step, meaning a purely empirical formula may lack physical meaning and fail to account for the characteristics of each aerosol type and the regional differences in meteorology.

A simple yet more explicit physically-based parametric wet scavenging scheme is embedded in the TE14 module to identify the rate of

wet removal for each particle. For the new parameterization, scavenging ratios for each aerosol type are diagnosed by comparing with the aerosol number concentrations before and after the microphysical process. To isolate the microphysical processes involved, we calculated the ratio of NWFA, NIFA, and BC before and after entering microphysical processes each time step, and assumed it as the same ratio for the removal of the associated aerosol species. For example, all related aerosols (sulfate, OC and sea salt) in the NWFA share the same removal ratio. Next, the aerosols are recalculated into mass concentration needed in the GOCART model. For aerosol sharing multi-size bins, their weights at each time step are also considered. For example, SEA2–4 are calculated separately in the chemistry module but combined in the microphysics module. The equation for converting number concentration to mass concentration can be described as follows:

$$chem_{sea_k,j+1} = \frac{aero_{sea_k,j+1}}{1E^{-6} \rho_{j+1}} \times \frac{N_{t_{sea2,j}} + N_{t_{sea3,j}} + N_{t_{sea4,j}}}{N_{t_{sea_k,j}}} \quad (6)$$

where $chem$ represents the mass concentration of aerosol species calculated in the chemistry process (units: $\mu\text{g}/\text{kg}$), $aero$ refers to the mass concentration participating in the microphysical process (units: g/m^3), k denotes the type of the sea salt ($k = 2,3,4$), ρ means the density of air (units: kg/m^3), N_t is the number concentrations (units: #/ g), and j and $j + 1$ refer to the aerosol concentrations before and after calculations in the TE14 scheme. A conversion factor of $1E^{-6}$ is used to translate units from $aero$ to $chem$. Similar calculations have been conducted for all the other thirteen aerosols. This approach enables the online evaluation of chemical species associated with bulk microphysics, including explicit cloud water, cloud droplet nucleation, and ice activation by aerosols. By implementing this adaptation of the standard WRF-Solar model, we minimize computational cost while incorporating an online aerosol-cloud-radiation model.

4. Experimental design and observations

4.1. Experiments design

The model is configured with a domain covering Eastern Asia at a 9 km horizontal resolution and 45 vertical levels, as depicted in Fig. 2a. The top of the model is located at 50 hPa. The initial and boundary conditions are derived from the NCEP-FNL (Final) Operational Global Analysis data, provided by the National Centers for Environmental Prediction (NCEP). This dataset offers global atmospheric fields on a $1^\circ \times 1^\circ$ grid, updated at 6-h intervals, and integrates observations from satellites, radiosondes, and surface stations to ensure high accuracy (<https://rda.ucar.edu/datasets/ds083.2/>, last accessed: 26 June 2024). It supplies key variables such as temperature, humidity, and wind components, driving the simulation with realistic, time-evolving atmospheric conditions. The anthropogenic aerosol emissions are considered

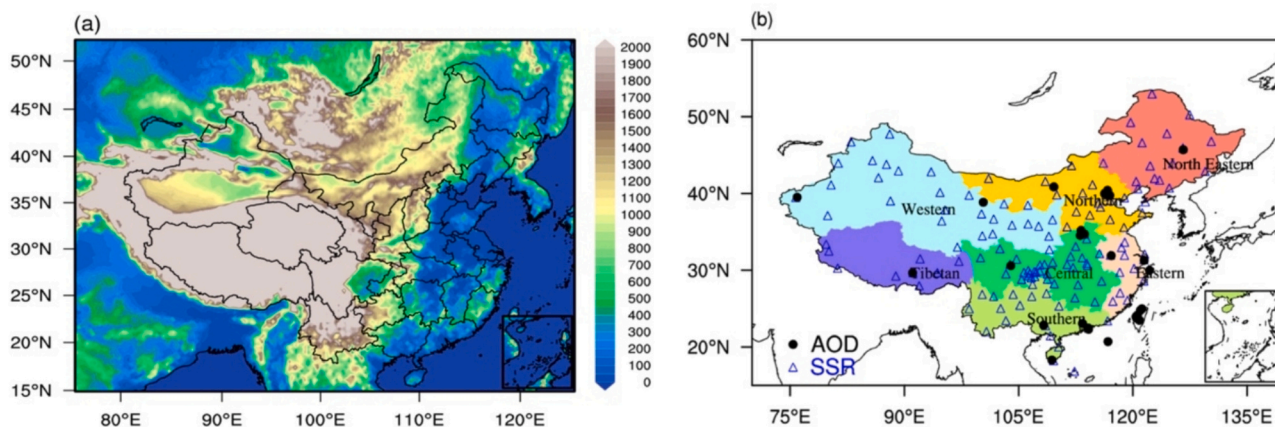


Fig. 2. (a) Simulation domain and terrain height (Units: meters), (b) The zoning map of seven main electricity grids in China in colors and the locations of the AOD and GHI monitoring network used in this study.

by using the latest HTAPv3 mosaic emission inventory for the year 2018 [47]. GOCART sea salt emissions are chosen in this study. The model time step is 30 s, with hourly gridded output to evaluate simulation performance.

The key physical and chemical parameterizations applied in the simulations are as follows: The effects of aerosol on the radiation simulation are calculated by the RRTMG [28]. The Mellor–Yamada–Nakanishi–Niino (MYNN2) scheme is used for the planetary boundary layer parameterization [48]. The moisture convective processes are parameterized by the Grell–Freitas scheme [49]. The Noah Land Surface Model is used to provide soil temperature and moisture in four layers [50]. The Air Force Weather Agency (AFWA) dust emission scheme is used [51], which has been demonstrated to well reveal the dust cycle [30,52]. A tuning ratio of 2 has been tested to provide the best dust simulation performance.

March 2021 is selected as the simulation period due to two significant dust events in North China: one from 14 to 18 March and another from 26 to 30 March, with the former being considered the most intensive dust event in China in the past 10 decade [53]. The simulation period spans from 26 February to 31 March 2021, with the first 6 days as “spin-up” time. The model is reinitialized daily using the meteorology field from FNL to maintain closeness to reality. Results from 4 to 31 March are analyzed here.

Two numerical experiments are conducted to examine the performance of the new aerosol wet scavenging in GHI simulation and the related variables in the WRF-Chem-Solar model. Details of the sensitivity tests are summarized in Table 2. The first experiment, named *Aero_Couple*, represents the fully coupled WRF-Chem-Solar with a physically-based aerosol wet scavenging scheme developed in this study. The second experiment *Aero_Half*, uses a simple wet scavenging scheme in the WRF-Chem-Solar model. Since the aerosol wet scavenging ratios are not affected by the aerosol-cloud process, it is therefore named *Aero_Half*. In our simulations, AOD is dynamically computed using modeled aerosol concentration profiles and their optical properties at 550 nm, ensuring comparability with observational data.

Table 2
Summary of the two experiments in this study.

Version	Aerosol dataset	Online Couple	Wet scavenging
<i>Aero_Couple</i>	Online calculation	✓	New wet scavenging scheme
<i>Aero_Half</i>	Online calculation	✓	wetscav_onoff = -1

4.2. Observations

4.2.1. AOD observations

AOD data are obtained from two ground-based networks: The Aerosol Robotic Network (AERONET) and the Sun–Sky Radiometer Observation Network (SONET). AERONET is a ground-based globally distributed remote sensing network designed for the automatic tracking of AOD over extended periods [54]. Data from the AERONET Version 3 aerosol retrieval algorithm, which has passed the quality control standard with an uncertainty of ± 0.01 , are used in this study [55]. Since AERONET does not retrieve the AOD at 550 nm (only at 340, 380, 440, 500, 675, 870, 1020, and 1640 nm), we employ the Ångström law to derive AOD at 550 nm from logarithmically interpolating the AOD at 440 and 675 nm. Subsequently, the AOD at 550 nm are averaged over 1-h intervals (30 min before and after each hour) to validate the model results. 19 stations are used in this study.

Additionally, 18 observation stations from SONET are included as supplementary data sources, with an average minor difference of 0.002 between the SONET and AERONET [56]. It provides AOD at nine channels with center wavelengths of 340, 380, 440, 550, 670, 870, 1020, and 1640 nm at every 15 min [56,57]. A similar interpolation method is applied to SONET data, and averages are calculated over 1-h intervals as well.

The AOD observations from AERONET and SONET are widely used as a benchmark for validating model performance by providing accurate, ‘ground-truth’ measurements of AOD [58–62]. Consequently, they are employed to assess the temporal performance of our model. The locations of all stations used can be found in Fig. 2b, indicated by black dots.

4.2.2. Moderate resolution imaging Spectroradiometer (MODIS) observations

The Moderate Resolution Imaging Spectroradiometer (MODIS) on-board Aqua and Terra satellites rotating Earth above 705 km. It provides global high-resolution cloud and aerosol optical properties every 1–2 days [63]. Previous studies have demonstrated a strong statistical relationship between MODIS data and AERONET L2 data [60,64], making MODIS a reliable source for global aerosol observations, particularly in regions lacking gridded ground-based data [65,66]. We used both Deep Blue (DB) and Dark Target (DT) combined AOD L2 collection 6.1 product at 550 nm from Aqua satellite (MYD04_L2) and Terra satellite (MOD04_L2) with the spatial resolution of $10 \text{ km} \times 10 \text{ km}$ at nadir [67,68]. Data from two satellites has been interpolated into the model grid and has been compared with the monthly mean AOD values of the model at the spatial scale.

4.2.3. Surface downward solar radiation compositions product (SSRC)

The distribution of GHI is evaluated using data from the Surface downward solar radiation compositions (SSRC) near real-time monitoring system, which is established over East Asia–Pacific with a spatial-temporal resolution of $0.05^\circ (10\text{min})^{-1}$ [69]. Derived from Himawari-8/9 and Fengyun-4 series data, it fully considers the effects of aerosol types, cloud phases, and gas components, and its accuracy of GHI (daily mean RMSEs of 19.7 W m^{-2}) are shown to be significantly better than those from CERES, ERA5, and GLASS [69]. The hourly scale GHI data (available from www.slrss.cn/care/sp/pc/, last access: 20 June 2024) is used to assess the model's capability to simulate the spatial distribution of GHI under both clear-sky and all-sky conditions during the study period. The GHI under clear sky are detected by the cloud type seen as clear.

4.2.4. Ground-based GHI observations

Observations of GHI across China from the China Meteorological Administration (CMA) are utilized for both all-sky and clear-sky scenarios. Following rigorous data quality control procedures [70,71], 138 sites are employed to validate the accuracy of the modeled GHI. The locations of all stations are depicted by blue triangles in Fig. 2b.

4.3. Validation methods

The absolute mean bias (BIAS), the root mean square error (RMSE), the correlation coefficient (CORR), and the index of agreement (IOA) are used to validate the model performance [72], the equation can be described as:

$$\text{BIAS} = \frac{1}{N-1} \sum_{i=1}^n (M_i - O_i) \quad (7)$$

$$\text{RMSE} = \sqrt{\frac{1}{N} \sum_{i=1}^n (M_i - O_i)^2} \quad (8)$$

$$\text{CORR} = \frac{\sum_{i=1}^n (M_i - \bar{M})(O_i - \bar{O})}{\sqrt{\sum_{i=1}^n (M_i - \bar{M})^2} \sqrt{\sum_{i=1}^n (O_i - \bar{O})^2}} \quad (9)$$

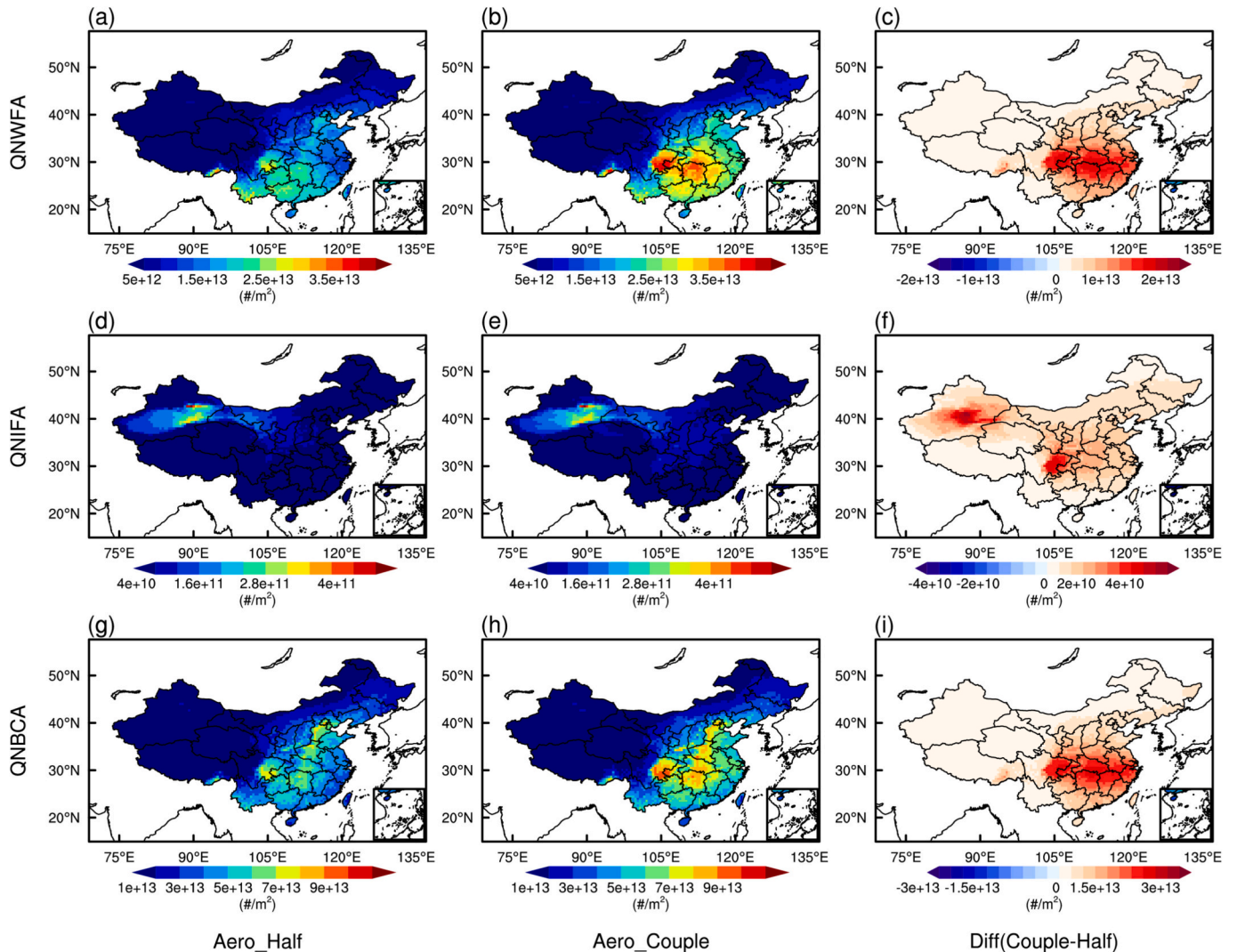


Fig. 3. Spatial distributions of the monthly mean number concentrations of vertically integrated water-friendly aerosol (QNWFA), ice-friendly aerosol (QNIFA) and black carbon aerosol (QNBCA) in the Aero_Couple (Left, a,d,g), Aero_Half (Middle, b,e,h) and their difference (Right, c,f,i) simulation from 4 to 31 March 2021, respectively, units: $\#/m^3$.

$$IOA = 1 - \frac{\sum_{i=1}^N (M_i - O_i)^2}{\sum_{i=1}^N (|O_i - \bar{O}| + |M_i - \bar{O}|)^2} \quad (10)$$

where M_i represents the simulations, O_i means the observed values, N is the total number of observations, \bar{M} and \bar{O} are the average values.

5. Results

5.1. The effects of aerosol wet scavenging on aerosol components

In the Aero_Couple and Aero_Half experiments, as the chemistry process is taken into consideration, the number concentrations of water-friendly aerosol (QNWFA), ice-friendly aerosol (QNIFA) and black carbon aerosol (QNBCA) are updated based on emissions and meteorological conditions. The spatial distributions of vertically integrated monthly mean number concentrations of the two experiments are presented in Fig. 3.

Due to the influence of the new aerosol wet scavenging scheme, the

distributions of QNWFA, QNIFA and QNBCA vary greatly between the two experiments. In the Aero_Couple simulation, QNWFA exhibits a broader high-value center in Sichuan, Hunan and adjacent regions (Fig. 3b), with values exceeding $4 \cdot 10^{13}/m^2$. In contrast, the Aero_Half simulation shows smaller high-value centers, with peak values around $3 \cdot 10^{13}/m^2$ in Southwest China. This discrepancy indicates the updated wet scavenging scheme is essential to increase QNWFA in southeast China, especially in Central China (Fig. 3c). This demonstrates the simple aerosol wet scavenging scheme overestimates the aerosol wet deposition. For QNIFA, the high number concentration values are predominantly found in northwestern China in the two experiments. Notable increases in Xinjiang and Sichuan provinces can be found in the Aero_Couple simulation, with values exceeding $4.5 \cdot 10^{10}/m^2$ (Fig. 3f). As for QNBCA, the high values center in southeastern China simulated in Aero_Half is much lower than that in the Aero_Couple simulation (Fig. 3g), simulation both experiments exhibiting comparable spatial patterns.

Then the spatial distributions of vertically integrated wet scavenging velocity and aerosol burdens for sulfate, OC, BC, and dust are examined in Fig. 4. Clearly, the high values centers of wet scavenging velocities for

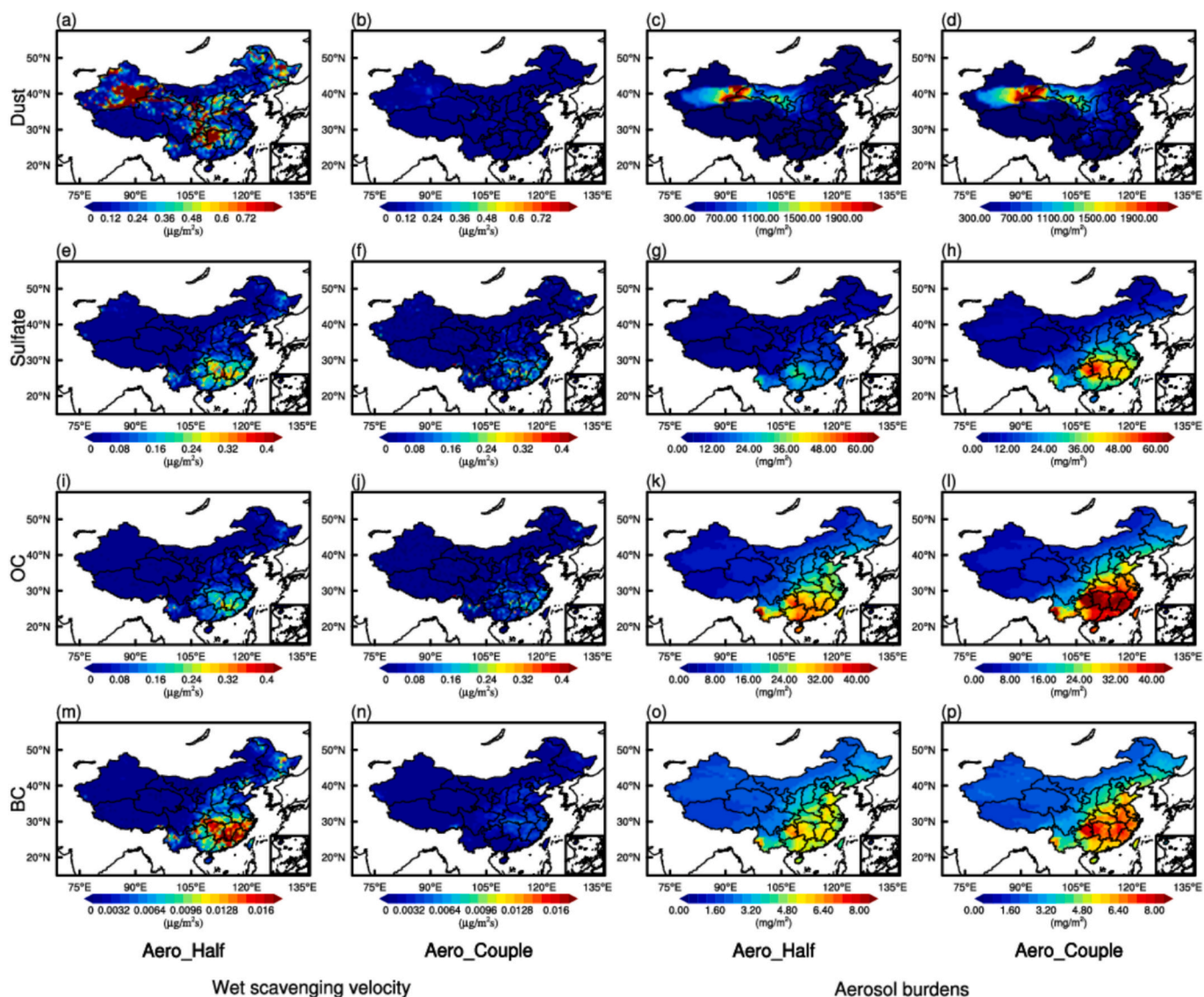


Fig. 4. Spatial distributions of the monthly mean vertically integrated wet scavenging velocity (units: $\mu g/m^2/s$) and aerosol burdens (units: mg/m^2) for each component (including dust, sulfate, organic carbon [OC], and black carbon [BC]) in the Aero_Couple and Aero_Half simulations from 4 to 31 March 2021, respectively.

sulfate aerosol, OC and BC are located in the Southeast coastal area, while the Aero_Half simulation exhibits stronger wet scavenging velocities (Fig. 4e, i, m). Meanwhile, high-value regions for dust, from Xinjiang to Hunan, are detected in Aero_Half in Fig. 4a. The reduced wet scavenging velocities in the Aero_Couple simulation result in less aerosol removal, leading to noticeable increases in aerosol burdens for each component.

For dust, a high-value center in Northwest China is simulated in both experiments, with high values over 2000 mg/m^2 in Gansu and Xinjiang provinces, reflecting the two major dust events that occurred in March 2021 (Fig. 4c, d). Additionally, the reduced wet scavenging velocities in the Aero_Couple experiment led to increased dust burdens from South Xinjiang to Guizhou. Similarly, after updating the wet scavenging scheme, increased sulfate aerosol, OC, and BC burdens are observed over southeastern China, with relative increases of 116.67 %, 37.69 % and 36.80 %, separately. The spatial distributions of near-surface aerosol burdens are broadly similar, with a notable increase in sulfate concentrations near coastal regions in the Aero_Couple experiment, reflecting the influence of an updated wet scavenging scheme in highly polluted areas (FigS. 1). Earlier studies have revealed a similar spatial distribution of sulfate, OC, and BC in March by MERRA-2 [73], which further validates the improvements introduced by the updated wet scavenging scheme.

5.2. The effects of aerosol wet scavenging on AOD

To evaluate the performance of the new aerosol wet scavenging scheme in reproducing AOD over China, the monthly mean spatial distributions of AOD in the two experiments are evaluated with MODIS in Fig. 5.

Clearly, as can be seen from MODIS results, the monthly mean AOD values across China in March 2021 typically range from 0.10 to over 1.50 (Fig. 5c), with higher values in both northwestern and coastal regions. Meanwhile, simulated AOD values fall within a broader range of 0.10 to over 2.00 (Fig. 5a-b). In regions affected by high anthropogenic aerosol levels, such as south of the Sichuan Basin, Northern and Southeast China, the results from Aero_Couple demonstrate a more accurate representation of AOD (beyond 0.80), attributed to the improved presence of sulfate, OC, and BC (Fig. 5b). In contrast, underestimated AOD in Southeastern China is found in the Aero_Half experiment

(Fig. 5a), indicating that the revised wet scavenging scheme considerably increase AOD by affecting aerosol burdens. Specifically, there are overestimated AOD values in Northwestern China (beyond 0.30) in both experiments, likely influenced by the dust schemes used. Earlier studies have found a similar overestimation of dust events in March 2021 in WRF-Chem [74,75], suggesting that tuning the ratio of the 10 m wind speed of FNL and the simulated 10 m wind speed could help further reduce the friction velocity and improve AOD results. This warrants further study. Compared to the Aero_Half experiment, the Aero_Couple experiment exhibits a widespread increase in AOD across China (Fig. 5f), with high-value centers in the northwestern and southeastern regions (exceeding 0.48). This pattern corresponds closely with the distribution of aerosol burdens (Fig. 4) and is partly attributed to difference in boundary layer height (BLH, FigS. 2). The Aero_Couple experiment shows lower BLH values across much of China, leading to elevated near-surface aerosol concentrations and higher AOD.

To further assess AOD performance across China, the results from 4 to 31 March 2021 are further divided into seven electricity regions [76], including Western China, Northeastern China, Eastern China, Northern China, Southern China, Central China, and the Tibetan Plateau (Tibetan), separately. The zoning map is shown in Fig. 2b with AOD observation locations. The time series of the regional averaged hourly simulated and observed (from AERONET and SONET) AOD are revealed in Fig. 6.

Although the simulated AOD is generally underestimated compared to the observed values, the evolution and magnitude of the AOD time series in dust-affected regions, such as Northern and Western China are reasonably reproduced by the Aero_Couple experiment during the simulation period. It accurately captures the heavy dust events happening on 14–17 March and 25–27 March in Northern China, with a CORR value of 0.66. Meanwhile, the event is underestimated in the Aero_Half experiment with a larger BIAS value below -0.64 . Compared to the Aero_Half experiment, the Aero_Couple experiment shows a relative decrease in RMSE and BIAS of 15.22 % and 20.31 %, respectively, in Northern China. Similar improvements are observed in Western China. In Central China, the Aero_Couple experiment significantly reduces BIAS from -0.21 to -0.02 , representing a relative decrease of 109.52 %, while the CORR value increases by 19.35 %. These results underscore the importance of updating aerosol removal in capturing the high AOD observed in March.

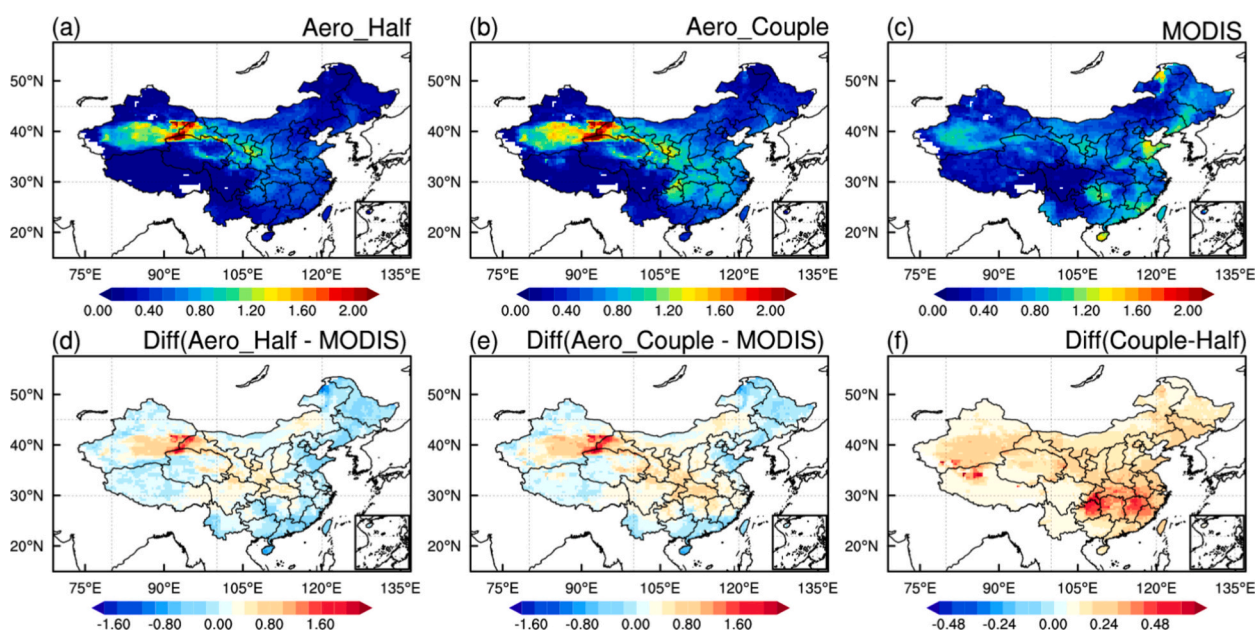


Fig. 5. Spatial distributions of the monthly mean AOD simulated in the (a) Aero_Half, (b) Aero_Couple, and (c) observations from MODIS and their differences (modeled minus observed ones, d-f) from 4 to 31 March 2021.

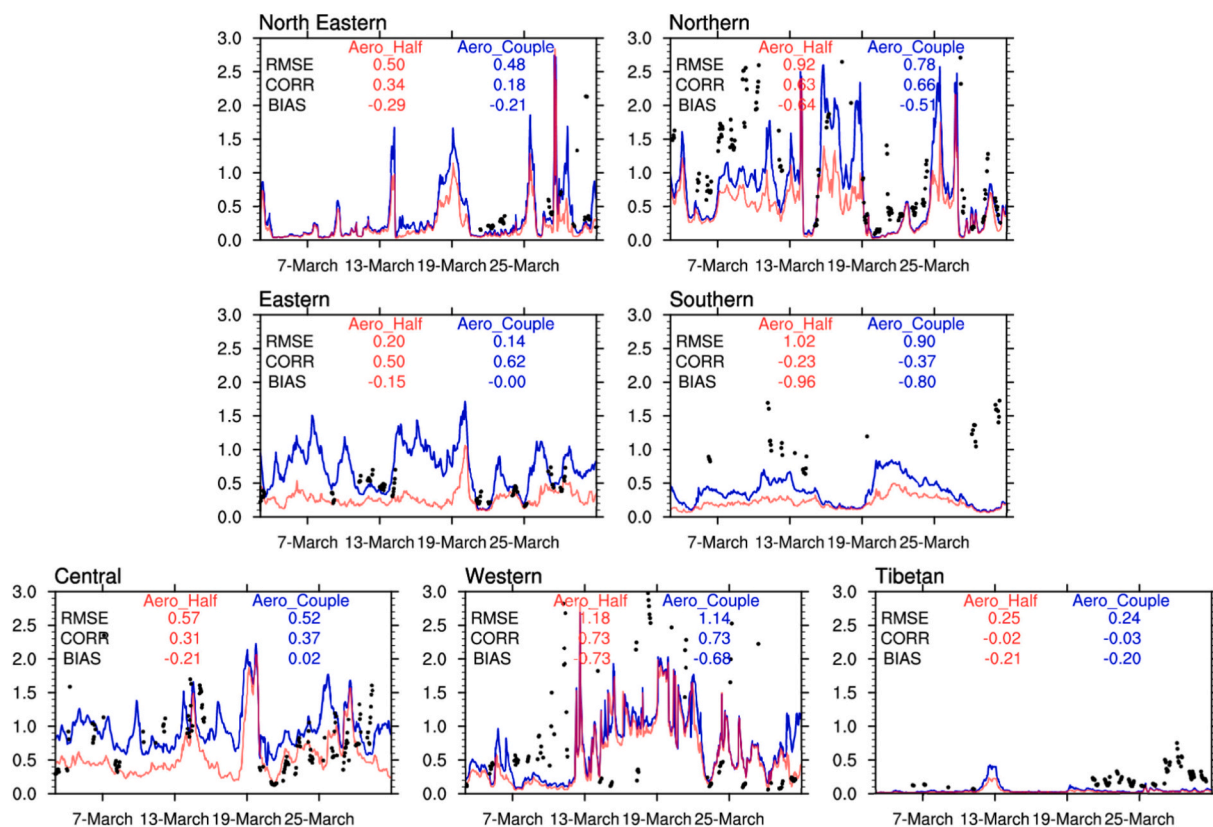


Fig. 6. Time series of the observed and simulated regional averaged hourly AOD in the Aero_Half and Aero_Couple experiments in seven electricity regions from 4 to 31 March 2021, the black dots represent the regional averaged observations.

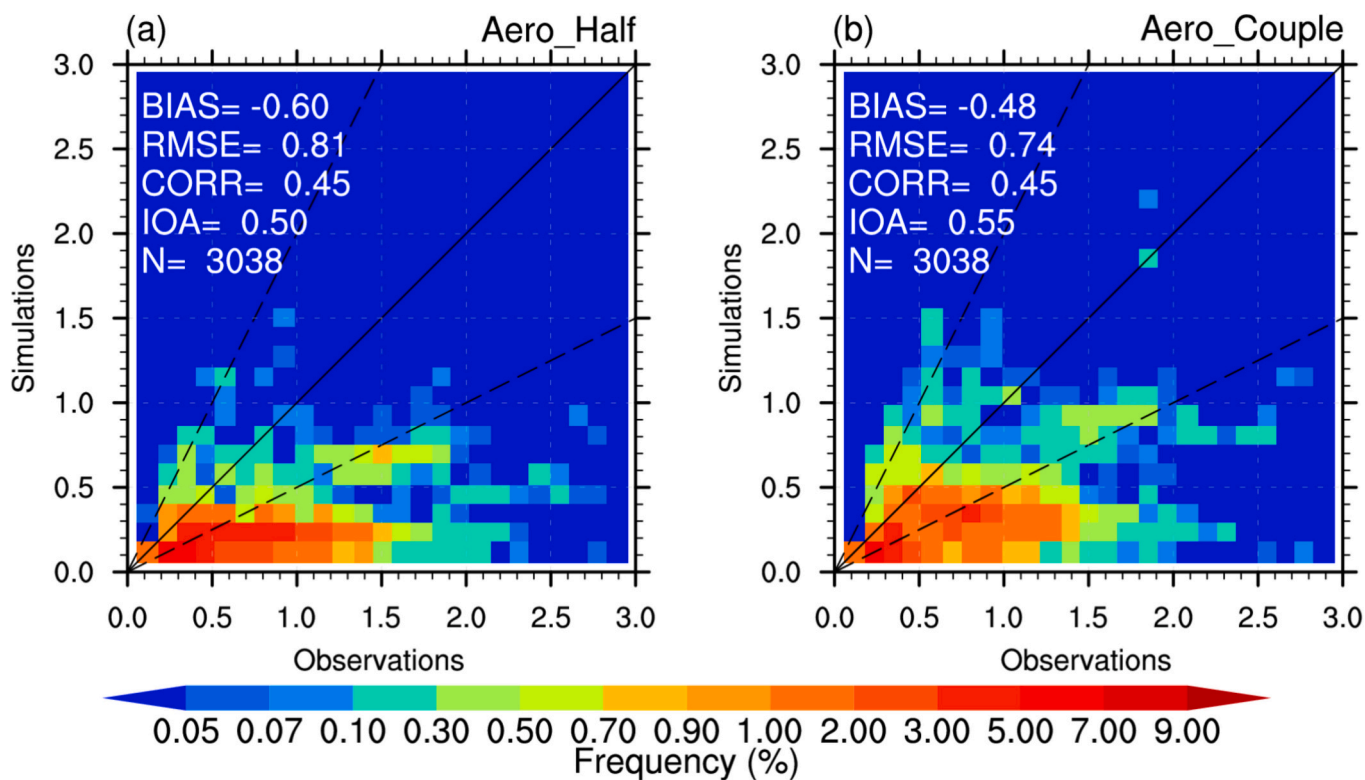


Fig. 7. Probability density distribution of the observed (from AERONET and SONET) AOD versus the simulated AOD in (a) Aero_Half and (b) Aero_Couple experiments, calculated at hourly scale from 4 to 31 March 2021. The continuous black line is the 1:1 line, and the dashed black lines correspond to the 1:2 and 2:1 lines. N shows the number of data used.

In Eastern China, significant improvement is detected in the Aero_Couple experiment, with the relative decrease of 30.00 % and 100.00 % for RMSE and BIAS, and an increase of 24.00 % for CORR compared with results from the Aero_Half experiment, respectively. In North Eastern China, although more data are needed to confirm the robustness of the results, the updated scheme reduces the excessive negative deviation by 27.59 % for BIAS. In Southern China, both experiments demonstrate poor performance, likely due to the lack of consideration of wildfire emissions, particularly in South Asia. Biomass-burning aerosols are a major contributor to the global burden of fine carbonaceous aerosols [26]. Observations indicate significant fires occurring in this region during spring will affect both air quality and AOD in China [77,78]. Additionally, both experiments fail to capture AOD variations in the Tibetan region. Similar underestimations have been observed in earlier studies, even when considering biomass burning emissions [79,80]. This may be linked to the absence of human-induced aerosols and the choice of dust parameterization schemes in that region [30], both of which need further study.

Subsequently, the simulated hourly AOD throughout March 4–31, 2021, is evaluated with all the observations in China, as depicted in Fig. 7. Clearly, both experiments show their strength in representing the time variation of AOD, with the same CORR value of 0.45. This performance is impacted by poor CORR values in North Eastern China and Southern China in the Aero_Couple experiment. The simulated AOD in the Aero_Half experiment shows higher BIAS and RMSE values of -0.60 and 0.81 (Fig. 7a), revealing a significant underestimation. After updating the aerosol removal scheme, the BIAS and RMSE values slightly decrease to -0.48 and 0.74 , respectively, which is consistent with smaller BIAS and RMSE values among seven regions in the Aero_Couple experiment. Meanwhile, a 10 % relative improvement in IOA value further supports the enhanced performance of the Aero_Couple experiment. Overall, the performance of Aero_Couple has improved across all evaluation indices, with more AOD data points aligning closely with the 1:1 line, resulting in 20.00 % decrease in BIAS values. The most notable enhancements can be observed in Central and Eastern China.

5.3. The effects of aerosol wet scavenging on GHI under clear skies

To evaluate the performance of the new aerosol wet scavenging scheme on GHI under clear sky, the spatial distribution of the monthly mean GHI under clear sky in two experiments and observations from SSRC, along with their differences, are depicted in Fig. 8.

Although both experiments underestimate the SSRC in parts of northwestern China due to overestimated dust emissions, they generally capture the spatial distribution (Fig. 8a, b). Additionally, since GHI under clear sky are primarily affected by aerosols, the positive biases (exceeding 25 W/m^2) observed in Inner Mongolia, North southern regions, North China plain, the coastal regions and Qinghai (Fig. 8d) are corrected in the Aero_Couple experiment (Fig. 8e), especially in regions with higher AOD (Fig. 5b). In general, the updating induces a decrease in GHI under clear sky across China, especially in Southeastern China (Fig. 8f), thus helping to improve the model performance in most regions of China.

To quantitatively assess the impact of the modification, time series of regional averaged observed and simulated GHI under clear sky are presented in Fig. 9. While the CORR values show limited improvement, due to the lower simulated BIAS values of AOD in the Aero_Couple experiment, significant reductions in BIAS and RMSE are observed across all regions. Notably, Central and Eastern China demonstrate remarkable decreasing BIAS values, with relative reductions of 104.30 % and 41.42 %, respectively. Meanwhile, although the AOD simulation shows weak improvement in western China, the BIAS of GHI under clear sky decreases by 45.70 %, likely due to the inconsistency in the number and location of AOD and SSRC observation sites. In Northern China, the new wet scavenging scheme contributes to 26.43 % and 12.73 % relative reductions in BIAS and RMSE values, respectively. Similar results have been detected in North Eastern and Southern China.

Fig. 10 further validates the model performance through probability density distributions. In the Aero_Couple experiment, more GHI under clear sky points align closely with the 1:1 line, reflecting a 36.47 % reduction in BIAS values compared to results in Aero_Half (Fig. 10b).

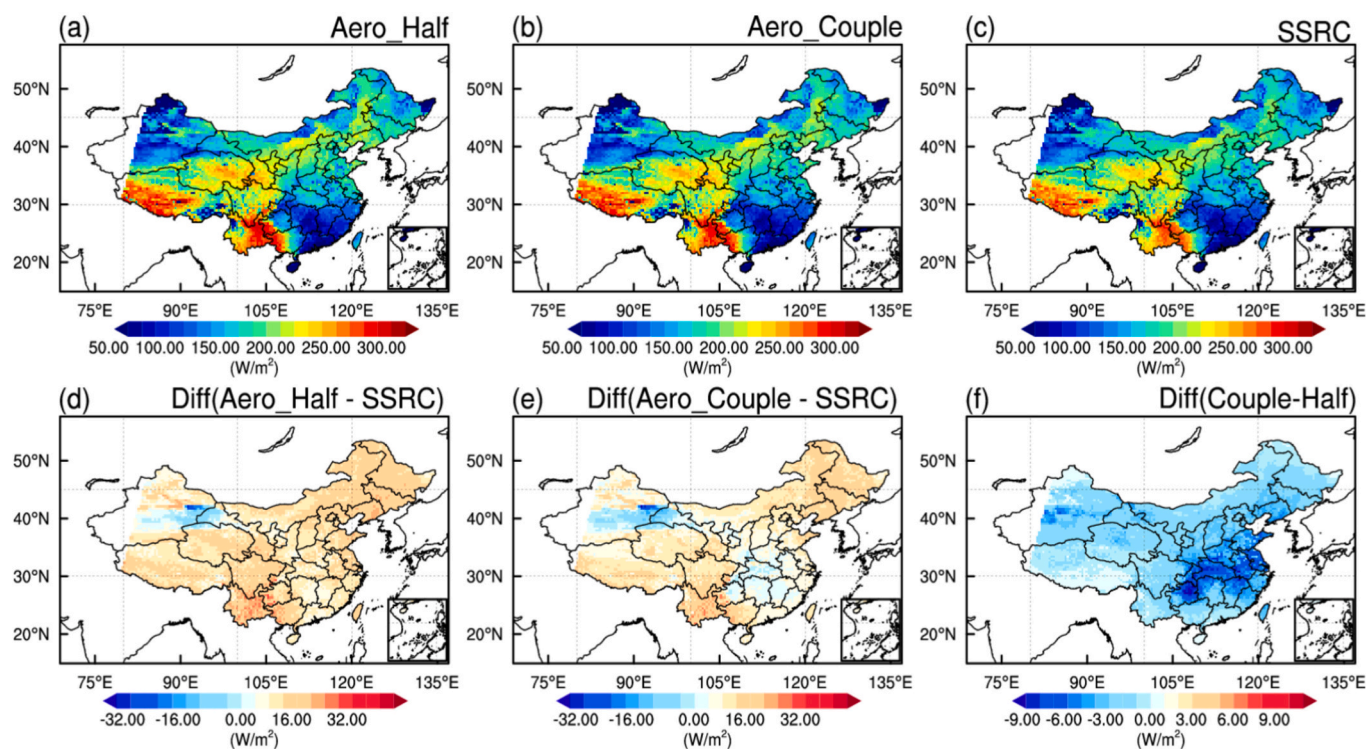


Fig. 8. Spatial distributions of the monthly mean GHI under clear sky in the (a) Aero_Half and (b) Aero_Couple simulations and their differences (d-e) compared with SSRC (modeled minus observed ones), respectively, the difference between the two experiments (f) from 4 to 31 March 2021 are also be given, units: W/m^2 .

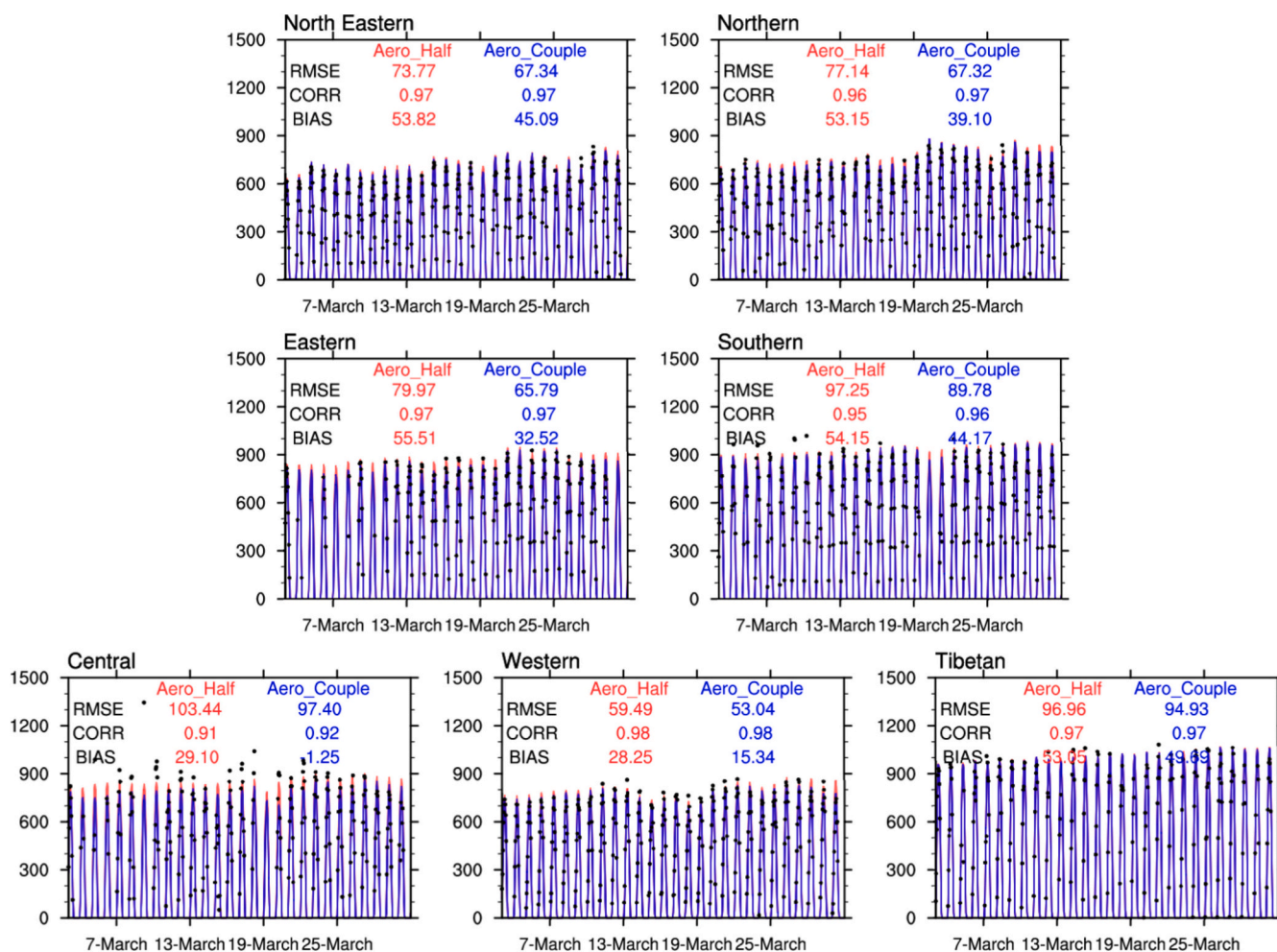


Fig. 9. Time series of the observed (ground-based GHI observations) and simulated regional averaged hourly GHI under clear sky in the Aero_Half and Aero_Couple experiments in seven electricity regions from 4 to 31 March 2021, the nighttime values have been removed before calculation. The black dots represent the regional averaged observations, units: W/m^2 .

Despite persistent underestimations of RMSE due to poor performance in Southern China and Tibetan, the updated scheme shows improved performance in high GHI zones ($>500 W/m^2$) under clear sky. BIAS values decrease from $33.49 W/m^2$ to $13.45 W/m^2$ with a relative reduction of 59.84%. In the ranges of $0-300 W/m^2$ and $300-500 W/m^2$, improvements are minor compared with the Aero_Half experiment. However, given the importance of high values of GHI under clear sky, these results indicate the essential role of updating aerosol wet removal in accurately simulating surface solar radiation. Diurnal variations of observed and simulated GHI under clear sky are given in Fig. 10d. Apparently, The Aero_Couple simulation better captures GHI under clear sky at 4–6 AM UTC, during which surface solar radiation is most abundant with the peak reaching $774.39 W/m^2$. The 24-h averaged AOD results (Fig. 10d) align with this pattern, showing a 47.44% reduction in the Aero_Half simulation compared to the updated model.

5.4. The effects of aerosol wet scavenging on GHI under all sky

Fig. 11 illustrates the spatial distribution of monthly mean GHI under all-sky conditions from both simulations as well as their difference compared to the result from the SSRC product. The Aero_Half simulation generally overestimates GHI under all-sky across most regions of China, except for the southeastern coastal areas and parts of northwestern China (Fig. 11d). These overestimations are partially corrected in the Aero_Couple simulation (Fig. 11e), resulting in GHI values that align more closely with observations. Notably, widespread reductions of GHI

under all-sky, particularly in southeastern China, are observed in the Aero_Couple experiment (Fig. 11f). The difference is consistent with the AOD distribution. As AOD increases in the Aero_Couple simulation, more scattering of GHI occurs, leading to the national decrease of the GHI. This phenomenon can be detected in the aerosol-direct influenced GHI (FigS. 3), which can partly explain the difference in Fig. 11f. Additionally, with the updating wet scavenging scheme, larger cloud optical thickness (COT) appears over China, especially in the southeastern regions (FigS. 4), which makes great contributions to the decreasing GHI under all sky.

Fig. 12 presents the time series of regional averaged GHI under all-sky conditions for the two experiments and observations. Consistent with results under clear-sky conditions, the Aero_Couple experiment achieves significantly lower BIAS and RMSE values across most regions in China. Among the seven regions, Central, Eastern, and Western China exhibit the most pronounced reductions in BIAS/RMSE, with relative decreases of 57.48%/18.35%, 50.62%/7.47%, and 32.40%/8.34%, respectively. The improvement is attributed to the noticeably larger COT over these regions (FigS. 4), which helps to reduce the significant positive deviation observed in the original model, especially for Central and Eastern China. These results highlight the effectiveness of the updated wet scavenging scheme in improving GHI simulations under all-sky conditions.

From the probability density functions plot across observations in China at an hourly scale in Fig. 13a-b, it is obvious that the BIAS value of GHI under all sky is reduced in the Aero_Couple experiment, with a

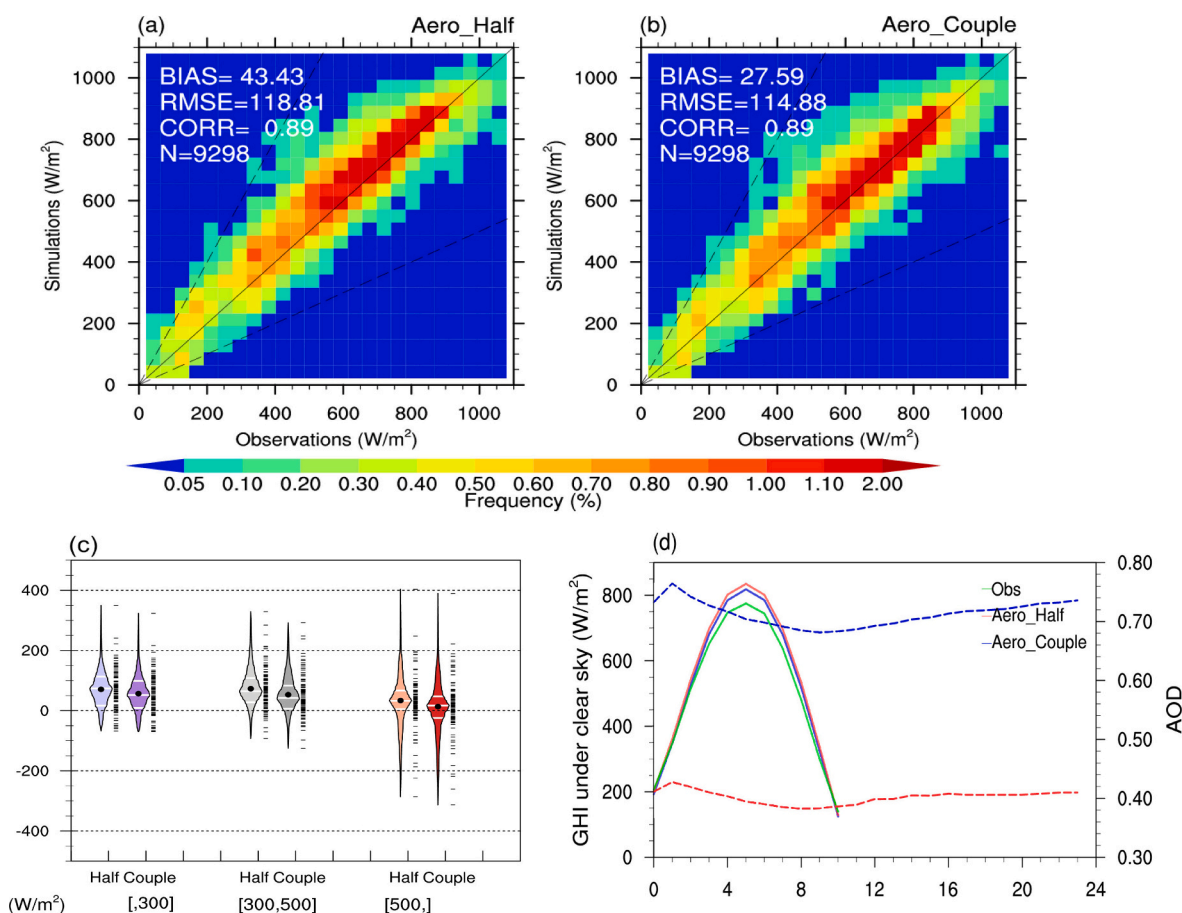


Fig. 10. Probability density distribution of the observed (ground-based GHI observations) versus the simulated GHI under clear sky in the (a) Aero_Half and (b) Aero_Couple experiments, calculated at hourly scale from 4 to 31 March 2021. The continuous black line is the 1:1 line, and the dashed black lines correspond to the 1:2 and 2:1 lines. (c) Box-percentile plots of the difference of the three experiments with the hourly observations, the nighttime values have been removed before calculation. Shapes of the plots indicating distributions of the biases, the black dots show the mean bias values of SSRC among all the stations in the three bins, units: W/m^2 , and (d) the diurnal variations of simulated and measured 24-h mean SSRC for all stations, the variations of AOD at the same stations are also given at dashed line.

relative reduction of 29.91 %. Additionally, the CORR value slightly increases from 0.81 to 0.82, driven by enhanced model performance in Eastern China. Overall, by perturbing the cloud optical thickness, the updated wet scavenging scheme will help to further reduce positive deviation in the model.

6. Summary and discussion

To scale back coal power and achieve net-zero carbon emissions, surface solar radiation stands out as a viable alternative with profound implications for future energy systems. The global horizontal irradiance (GHI) under clear-sky and all-sky conditions is a critical variable in most surface solar radiation prediction and simulation systems. However, the simulation and inversion capabilities are constrained by the substantial uncertainties associated with aerosol-cloud processes in models, especially under all-sky conditions.

In this study, a fully online coupled aerosol-cloud-radiation interaction is developed in the WRF-Solar model by interacting the TE14 microphysics scheme with the GOCART model (referred to as WRF-Chem-Solar), incurring a limited increase in computational time. Then the effect of a new physical-based parametric wet scavenging scheme on GHI has been quantified and evaluated. March 2021 is selected as the simulation period due to its inclusion of two significant dust events in

Northern China. Two experiments, Aero_Half and Aero_Couple, are conducted to assess the performance of the updated aerosol wet scavenging scheme on GHI and related variables at an hourly scale within the WRF-Chem-Solar model.

The results demonstrate that updating the wet removal process for aerosols reduces wet removal velocities and yields more realistic simulations of aerosol component burdens, effectively capturing the evolution and magnitude of QNWFA, QNIFA, and QNBCA. In Southeastern China, relative reductions of wet removal rates for sulfate, organic carbon (OC), and black carbon (BC) are observed at 116.67 %, 37.69 %, and 36.80 %, respectively.

Furthermore, the spatial patterns of mean AOD over China during the simulation period are compared with MODIS and observations. High-value centers in Northwestern China, the North China Plain, the southern Sichuan Basin, and Southeastern China are effectively represented in the Aero_Couple experiment. Additionally, the severe dust events of March 14–17 and March 25–27 in Western and Northern China are accurately captured. Consistent improvements in AOD simulations are observed across most regions of China, except for Southern China and Tibet. Nationally, the BIAS value decreases by 20.00 %, and the IOA values improve by 10.00 % at an hourly scale compared to Aero_Half results.

The reduction in negative BIAS values for AOD leads to corrections of

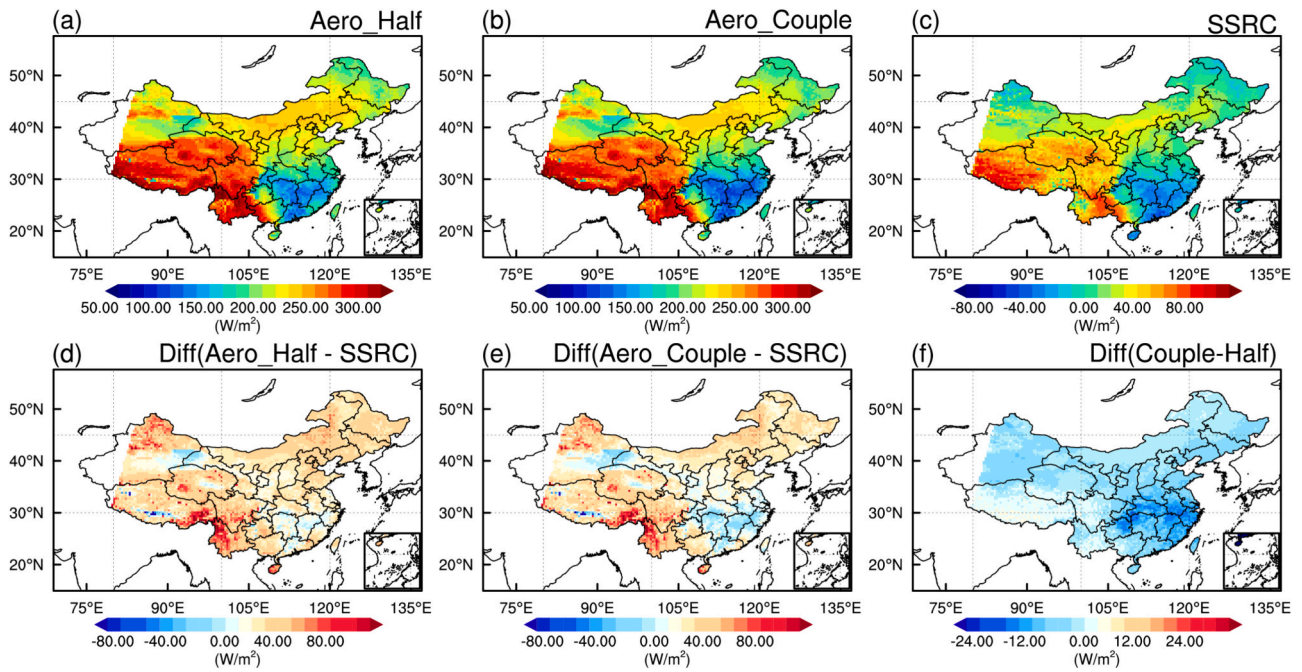


Fig. 11. Spatial distributions of the monthly mean GHI under all-sky in the (a) Aero_Half and (b) Aero_Couple simulations and their differences (d-e) compared with SSRC (modeled minus observed ones), respectively, the difference between the two experiments (f) from 4 to 31 March 2021 are also be given, units: W/m².

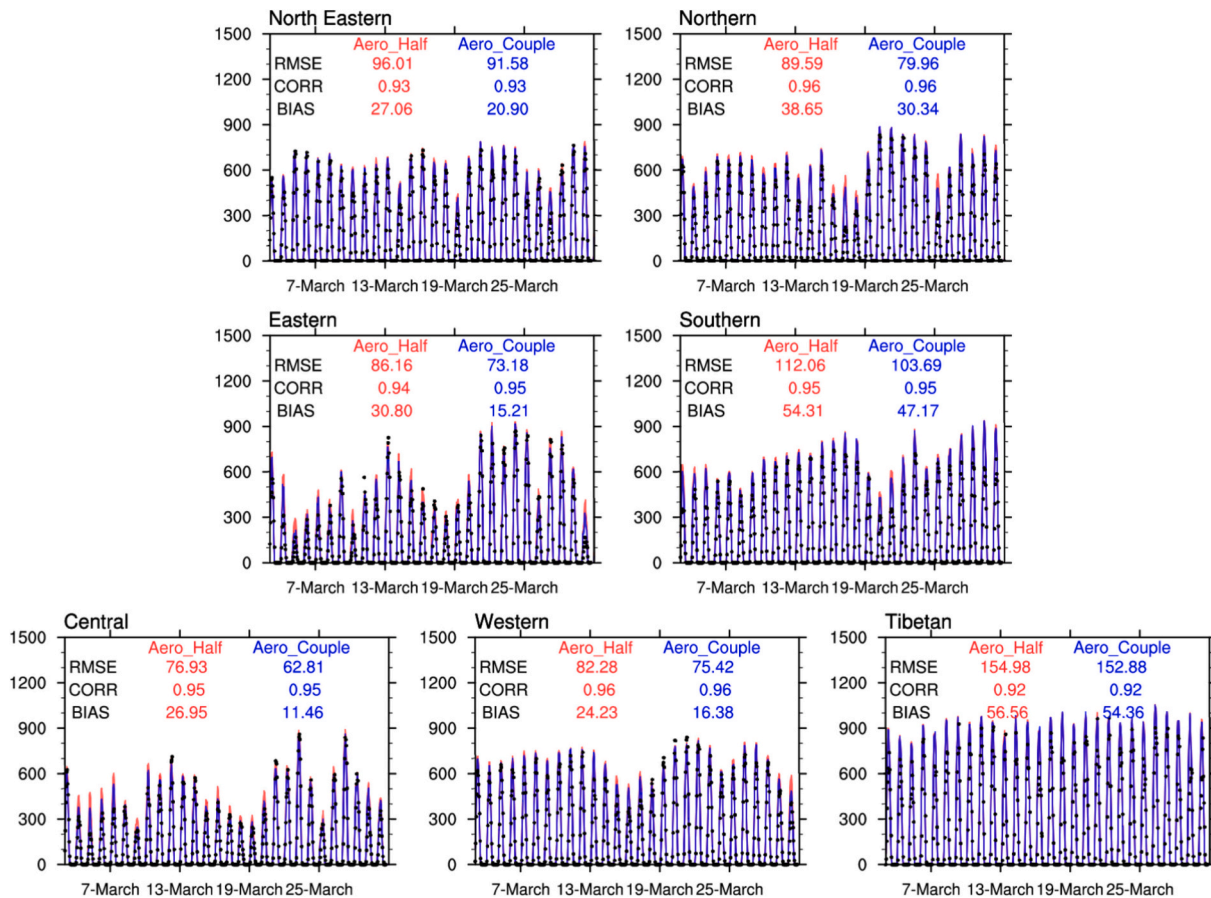


Fig. 12. Time series of the observed and simulated regional averaged hourly GHI under all-sky in the Aero_Half and Aero_Couple experiments in seven electricity regions from 4 to 31 March 2021, the nighttime values have been removed before calculation. The black dots represent the regional averaged observations, units: W/m².

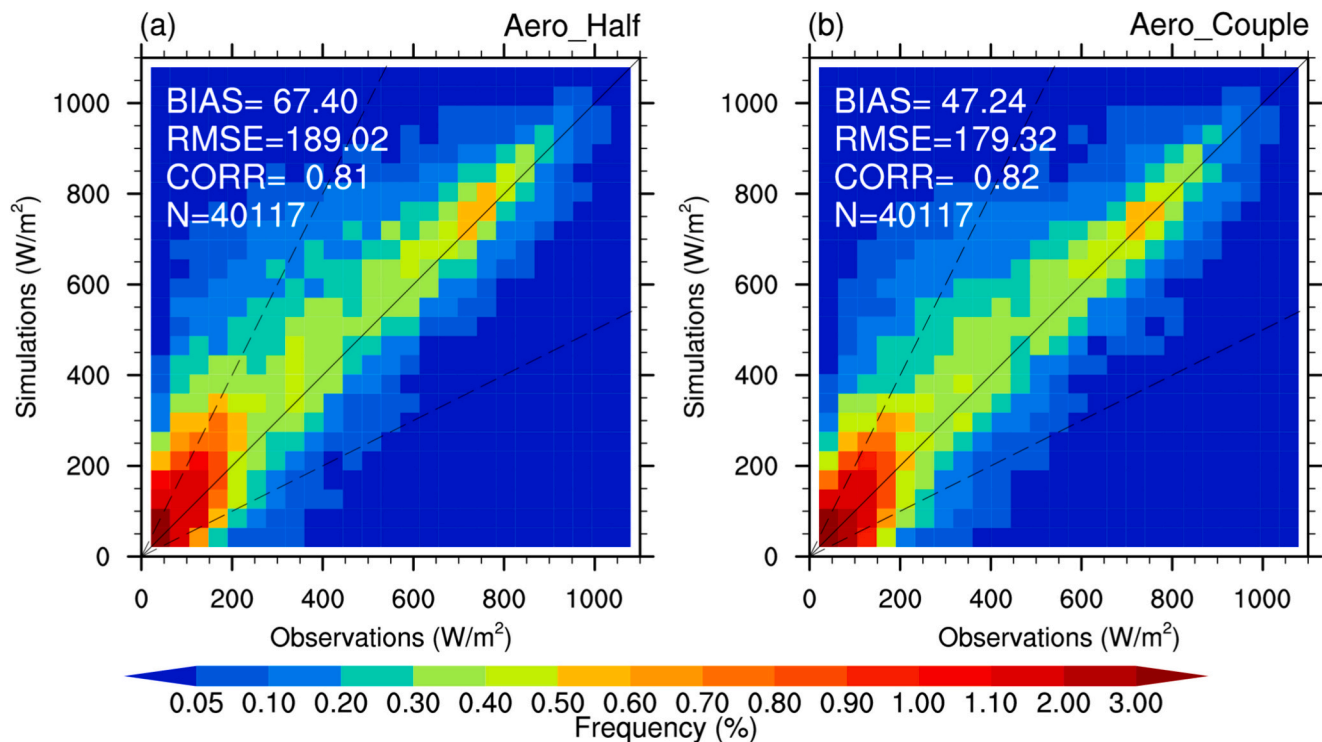


Fig. 13. Probability density distribution of the observed versus the simulated GHI under all-sky in the (a) Aero_Half and (b) Aero_Couple experiments, calculated at hourly scale from 4 to 31 March 2021. The nighttime values have been removed before calculation. The continuous black line is the 1:1 line, and the dashed black lines correspond to the 1:2 and 2:1 lines.

excessive GHI overestimations under clear-sky conditions in the Aero_Half experiment. Simulation results for Inner Mongolia, the North China Plain, southern regions, the coastal areas, and Qinghai are significantly closer to reality. Notably, BIAS values decrease across all regions in China except for Southern China and Tibet, with a national relative improvement of 36.47 %. High GHI zones ($GHI > 500 \text{ W/m}^2$) under clear sky show notable enhancements, with mean BIAS reduced by 59.84 %. The most pronounced improvements in BIAS are observed in Central, Western, and Eastern China, with relative improvements of 104.30 %, 45.70 %, and 41.42 %, respectively. Similar improvement is evaluated for GHI under all-sky, with a national relative improvement of 29.91 %. Central, Eastern, and Western China exhibit the most significant BIAS reductions, with relative decreases of 57.48 %, 50.62 %, and 32.40 %, respectively. These results underscore the essential role of updating aerosol wet scavenging schemes in the WRF-Chem-Solar model.

This work mainly focused on the development of aerosol wet scavenging schemes in the WRF-Chem-Solar model and its performance on GHI simulation. Future work should include an evaluation with the original version of WRF-Chem, and more cases are needed to further verify the applied effect of this scheme on more variables and other seasons. A series of tuning works is needed to reduce the uncertainty of AOD in Northwestern China. Furthermore, since the experiments lack consideration of wildfire emissions, integrating them to intelligently extract the characteristics of wildfire-related events in South Asia will be crucial.

Authors contribution

Su Wang provided the draft of the manuscript. Gang Huang guided the paper structure. Tie Dai provided the conceptualization. Junji Cao edited the draft of the manuscript. Letu Husi and Run Ma made contributions to the SSRC data used. Cuina Li made contributions to the observation data used.

CRediT authorship contribution statement

Su Wang: Writing – original draft. **Gang Huang:** Funding acquisition, Conceptualization. **Tie Dai:** Conceptualization. **Junji Cao:** Supervision. **Letu Husi:** Data curation. **Run Ma:** Data curation. **Cuina Li:** Data curation.

Declaration of competing interest

The authors declare that they have no known competing financial interests or personal relationships that could have appeared to influence the work reported in this paper.

Acknowledgments

The study was supported jointly by the National Natural Science Foundation of China (Grant No. 42305202), the National Natural Science Foundation of China (Grant No. 42141019, 42261144687, 42430611, 42405145), the CAS proof-of-concept program (grant no. CAS-GNYZ-2022), the Natural Science Foundation of Sichuan Province (2024NSFSC0770).

Appendix A. Supplementary data

Supplementary data to this article can be found online at <https://doi.org/10.1016/j.apenergy.2025.126062>.

Data availability

The authors do not have permission to share data.

References

- [1] United Nations Environment Programme FS of F and M BloombergNEF. Global Trends in Renewable Energy Investment 2020. 2020.

- [2] Shi H, Yang D, Wang W, Fu D, Gao L, Zhang J, et al. First estimation of high-resolution solar photovoltaic resource maps over China with Fengyun-4A satellite and machine learning. *Renew Sust Energ Rev* 2023;184:113549. <https://doi.org/10.1016/j.rser.2023.113549>.
- [3] Diagne M, David M, Lauret P, Boland J, Schmutz N. Review of solar irradiance forecasting methods and a proposition for small-scale insular grids. *Renew Sust Energ Rev* 2013;27:65–76. <https://doi.org/10.1016/j.rser.2013.06.042>.
- [4] Rodríguez-Benítez FJ, Arbizu-Barrena C, Huertas-Tato J, Aler-Mur R, Galván-León I, Pozo-Vázquez D. A short-term solar radiation forecasting system for the Iberian Peninsula. Part 1: models description and performance assessment. *Sol Energy* 2020;195:396–412. <https://doi.org/10.1016/j.solener.2019.11.028>.
- [5] Zhong X, Ruiz-Arias JA, Kleissl J. Dissecting surface clear sky irradiance bias in numerical weather prediction: application and corrections to the new Goddard shortwave scheme. *Sol Energy* 2016;132:103–13. <https://doi.org/10.1016/j.solener.2016.03.009>.
- [6] Jimenez PA, Hacker JP, Dudhia J, Haupt SE, Ruiz-Arias JA, Gueymard CA, et al. WRF-solar: description and clear-sky assessment of an augmented NWP model for solar power prediction. *Bull Am Meteorol Soc* 2016;97:1249–64. <https://doi.org/10.1175/BAMS-D-14-00279.1>.
- [7] IPCC. Climate Change 2021: The Physical Science Basis. In: Contribution of Working Group I to the Sixth Assessment Report of the Intergovernmental Panel on Climate Change; 2021. <https://doi.org/10.1017/9781009157896>. In Press.
- [8] Ramanathan V, Crutzen P, Kiehl J, Rosenfeld D. Atmosphere - aerosols, climate, and the hydrological cycle. *Science* 2001;294:2119–24. <https://doi.org/10.1126/science.1064034>.
- [9] Liu L, Yuan H, Deng Y, Ren J, Bai Y, Cui C. Effects of aerosols on the forecasting of Mei-yu frontal storms over the Yangtze–Huai River valley. *Atmos Res* 2023;283:106535. <https://doi.org/10.1016/j.atmosres.2022.106535>.
- [10] Yang H, Xiao H, Guo C, Wen G, Tang Q, Sun Y. Comparison of aerosol effects on simulated spring and summer hailstorm clouds. *Adv Atmos Sci* 2017;34:877–93. <https://doi.org/10.1007/s00376-017-6138-y>.
- [11] Zhang Y, Gao Y, Guo L, Zhang M. Numerical analysis of aerosol direct and indirect effects on an extreme rainfall event over Beijing in July 2016. *Atmos Res* 2021;264:105871. <https://doi.org/10.1016/j.atmosres.2021.105871>.
- [12] Razagui A, Abdeladim K, Bouchouicha K, Bachari N, Semaoui S, Hadj Arab A. A new approach to forecast solar irradiances using WRF and libRadtran models, validated with MERRA-2 reanalysis data and pyranometer measures. *Sol Energy* 2021;221:148–61. <https://doi.org/10.1016/j.solener.2021.04.024>.
- [13] Croft B, Lohmann U, Martin RV, Stier P, Wurzel S, Feichter J, et al. Influences of in-cloud aerosol scavenging parameterizations on aerosol concentrations and wet deposition in ECHAM5-HAM. *Atmos Chem Phys* 2010;10:1511–43. <https://doi.org/10.5194/acp-10-1511-2010>.
- [14] Ryu Y-H, Min S-K. Improving wet and dry deposition of aerosols in WRF-Chem: updates to below-cloud scavenging and coarse-particle dry deposition. *J Adv Model Earth Syst* 2022;14:e2021MS002792. <https://doi.org/10.1029/2021MS002792>.
- [15] Rasch PJ, Barth MC, Kiehl JT, Schwartz SE, Benkovitz CM. A description of the global sulfur cycle and its controlling processes in the National Center for Atmospheric Research Community climate model, version 3. *J Geophys Res Atmos* 2000;105:1367–85. <https://doi.org/10.1029/1999JD900777>.
- [16] Tie X, Madronich S, Walters S, Edwards DP, Ginoux P, Mahowald N, et al. Assessment of the global impact of aerosols on tropospheric oxidants. *J Geophys Res Atmos* 2005;110. <https://doi.org/10.1029/2004JD005359>.
- [17] Li Y, Pickering KE, Barth MC, Bela MM, Cummings KA, Allen DJ. Wet scavenging in WRF-Chem simulations of parameterized convection for a severe storm during the DC3 field campaign. *J Geophys Res Atmos* 2019;124:7413–28. <https://doi.org/10.1029/2019JD030484>.
- [18] Thompson G, Eidhammer T. A study of aerosol impacts on clouds and precipitation development in a large winter cyclone. *J Atmos Sci* 2014;71:3636–58. <https://doi.org/10.1175/JAS-D-13-0305.1>.
- [19] Zhang G, Ma Y. Clear-sky surface solar radiation and the radiative effect of aerosol and water vapor based on simulations and satellite observations over northern China. *Remote Sens* 2020;12. <https://doi.org/10.3390/rs12121931>.
- [20] Tegen I, Hollrig P, Chin M, Fung I, Jacob D, Penner J. Contribution of different aerosol species to the global aerosol extinction optical thickness: estimates from model results. *J Geophys Res-Atmos* 1997;102:23895–915. <https://doi.org/10.1029/97JD01864>.
- [21] Guo C, Chen D, Chen M, Zhang S, Guo J, Ma Z. Aerosol impacts on summer precipitation forecast over the North China plain by using Thompson aerosol-aware scheme in WRF: statistical analysis and significant threat score improvements in polluted condition during June to August 2018. *Atmos Res* 2024;299:107177. <https://doi.org/10.1016/j.atmosres.2023.107177>.
- [22] Gentile S, Di Paola F, Cimini D, Gallucci D, Gerdali E, Larosa S, et al. 3D-VAR data assimilation of SEVIRI radiances for the prediction of solar irradiance in Italy using WRF solar mesoscale model—preliminary results. *Remote Sens* 2020;12:920. <https://doi.org/10.3390/rs12060920>.
- [23] Jiménez PA, Yang J, Kim J-H, Sengupta M, Dudhia J. Assessing the WRF-solar model performance using satellite-derived irradiance from the National Solar Radiation Database. *J Appl Meteorol Climatol* 2022;61:129–42. <https://doi.org/10.1175/JAMC-D-21-0090.1>.
- [24] Weston MJ, Piketh SJ, Burnet F, Broccardo S, Denjean C, Bourrienne T, et al. Sensitivity analysis of an aerosol-aware microphysics scheme in weather research and forecasting (WRF) during case studies of fog in Namibia. *Atmos Chem Phys* 2022;22:10221–45. <https://doi.org/10.5194/acp-22-10221-2022>.
- [25] Li C, Mao J, Lau K, Chen J, Yuan Z, Liu X, et al. Characteristics of distribution and seasonal variation of aerosol optical depth in eastern China with MODIS products. *Chin Sci Bull* 2003;48:2488–95.
- [26] Saide PE, Thompson G, Eidhammer T, da Silva AM, Pierce RB, Carmichael GR. Assessment of biomass burning smoke influence on environmental conditions for multiyear tornado outbreaks by combining aerosol-aware microphysics and fire emission constraints. *J Geophys Res Atmos* 2016;121:10,294–10,311. <https://doi.org/10.1002/2016JD025056>.
- [27] Chou M-D, Suarez MJ. A solar radiation parameterization for atmospheric studies. 1999.
- [28] Iacono MJ, Delamere JS, Mlawer EJ, Shephard MW, Clough SA, Collins WD. Radiative forcing by long-lived greenhouse gases: calculations with the AER radiative transfer models. *J Geophys Res-Atmos* 2008;113:D13103. <https://doi.org/10.1029/2008JD009944>.
- [29] Wang S, Dai T, Li C, Cheng Y, Huang G, Shi G. Improving clear-sky solar power prediction over China by assimilating Himawari-8 aerosol optical depth with WRF-Chem-solar. *Remote Sens* 2022;14:4990. <https://doi.org/10.3390/rs14194990>.
- [30] Su L, Fung JCH. Investigating the role of dust in ice nucleation within clouds and further effects on the regional weather system over East Asia – part 1: model development and validation. *Atmos Chem Phys* 2018;18:8707–25. <https://doi.org/10.5194/acp-18-8707-2018>.
- [31] Barbaro EW. Interactions between aerosol and convective boundary-layer dynamics over land. phd. Wageningen University; 2015.
- [32] Ruiz-Arias JA, Dudhia J, Gueymard CA. A simple parameterization of the short-wave aerosol optical properties for surface direct and diffuse irradiances assessment in a numerical weather model. *Geosci Model Dev* 2014;7:1159–74. <https://doi.org/10.5194/gmd-7-1159-2014>.
- [33] Grell GA, Peckham SE, Schmitz R, McKeen SA, Frost G, Skamarock WC, et al. Fully coupled “online” chemistry within the WRF model. *Atmos Environ* 2005;39:6957–75. <https://doi.org/10.1016/j.atmosenv.2005.04.027>.
- [34] Chapman EG, Gustafson WI, Easter RC, Barnard JC, Ghan SJ, Pekour MS, et al. Coupling aerosol-cloud-radiative processes in the WRF-Chem model: investigating the radiative impact of elevated point sources. *Atmos Chem Phys* 2009;9:945–64. <https://doi.org/10.5194/acp-9-945-2009>.
- [35] Auligné T. Multivariate minimum residual method for cloud retrieval. Part I: theoretical aspects and simulated observation experiments. *Mon Weather Rev* 2014;142:4383–98. <https://doi.org/10.1175/MWR-D-13-00172.1>.
- [36] Auligné T. Multivariate minimum residual method for cloud retrieval. Part II: real observations experiments. *Mon Weather Rev* 2014;142:4399–415. <https://doi.org/10.1175/MWR-D-13-00173.1>.
- [37] Deng A, Gaudet B, Dudhia Alapaty K. Implementation and evaluation of a new shallow convection scheme in WRF. In: Atlanta, GA: 94th American Meteorological Society annual Meeting, 26th conference on weather analysis and forecasting/22nd conference on numerical weather prediction; 2014.
- [38] Ginoux P, Chin M, Tegen I, Prospero JM, Holben B, Dubovik O, et al. Sources and distributions of dust aerosols simulated with the GOCART model. *J Geophys Res Atmos* 2001;106:20255–73. <https://doi.org/10.1029/2000JD000053>.
- [39] Chin M, Ginoux P, Kinne S, Torres O, Holben BN, Duncan BN, et al. Tropospheric aerosol optical thickness from the GOCART model and comparisons with satellite and Sun photometer measurements. *J Atmos Sci* 2002;59:461–83. [https://doi.org/10.1175/1520-0469\(2002\)059<0461:TAOTFT>2.0.CO;2](https://doi.org/10.1175/1520-0469(2002)059<0461:TAOTFT>2.0.CO;2).
- [40] DeMott PJ, Prenni AJ, Liu X, Kreidenweis SM, Petters MD, Twohy CH, et al. Predicting global atmospheric ice nuclei distributions and their impacts on climate. *Proc Natl Acad Sci USA* 2010;107:11217–22. <https://doi.org/10.1073/pnas.0910818107>.
- [41] Boucher O, Anderson TL. General circulation model assessment of the sensitivity of direct climate forcing by anthropogenic sulfate aerosols to aerosol size and chemistry. *J Geophys Res Atmos* 1995;100:26117–34. <https://doi.org/10.1029/95JD02531>.
- [42] Qiao X, Tang Y, Hu J, Zhang S, Li J, Kota SH, et al. Modeling dry and wet deposition of sulfate, nitrate, and ammonium ions in Jiuzhaigou National Nature Reserve, China using a source-oriented CMAQ model: Part I. Base case model results. *Sci Total Environ* 2015;532:831–9. <https://doi.org/10.1016/j.scitotenv.2015.05.108>.
- [43] Stier P, Feichter J, Kinne S, Kloster S, Vignati E, Wilson J, et al. The aerosol-climate model ECHAM5-HAM. *Atmos Chem Phys* 2005;5:1125–56. <https://doi.org/10.5194/acp-5-1125-2005>.
- [44] Hess M, Koepke P, Schult I. Optical properties of aerosols and clouds: the software package OPAC. *Bull Am Meteorol Soc* 1998;79:831–44. [https://doi.org/10.1175/1520-0477\(1998\)079<0831:OPOAAC>2.0.CO;2](https://doi.org/10.1175/1520-0477(1998)079<0831:OPOAAC>2.0.CO;2).
- [45] Tegen I, Fung I. Modeling of mineral dust in the atmosphere: sources, transport, and optical thickness. *J Geophys Res Atmos* 1994;99:22897–914. <https://doi.org/10.1029/94JD01928>.
- [46] Deepak A, Gerber HE, Organization (WMO) WM. E meeting on aerosols and their climatic effects (28–30). Report of the experts meeting on aerosols and their climatic effects n.d. <https://library.wmo.int/records/item/36979-report-of-the-experts-meeting-on-aerosols-and-their-climatic-effects>. [Accessed 11 February 2025].
- [47] Crippa M, Guizzardi D, Butler T, Keating T, Wu R, Kaminski J, et al. The HTAP v3 emission mosaic: merging regional and global monthly emissions (2000–2018) to support air quality modelling and policies. *Earth SystSci Data* 2023;15:2667–94. <https://doi.org/10.5194/essd-15-2667-2023>.
- [48] Nakanishi M, Niino H. An Improved Mellor–Yamada Level-3 Model: Its Numerical Stability and Application to a Regional Prediction of Advection Fog. *Bound-Layer Meteorol* 2006;119:397–407. <https://doi.org/10.1007/s10546-005-9030-8>.
- [49] Grell GA, Freitas SR. A scale and aerosol aware stochastic convective parameterization for weather and air quality modeling. *Atmos Chem Phys* 2014;14:5233–50. <https://doi.org/10.5194/acp-14-5233-2014>.

- [50] Schaake JC, Koren VI, Duan Q-Y, Mitchell K, Chen F. Simple water balance model for estimating runoff at different spatial and temporal scales. *J Geophys Res Atmos* 1996;101:7461–75. <https://doi.org/10.1029/95JD02892>.
- [51] Jones SL, Adams-Selin R, Hunt ED, Creighton GA, Cetola JD. Update on modifications to WRF-CHEM GOCART for fine-scale dust forecasting at AFWA 2012. 2012. A33D-0188.
- [52] LeGrand SL, Polashenski C, Letcher TW, Creighton GA, Peckham SE, Cetola JD. The AFWA dust emission scheme for the GOCART aerosol model in WRF-Chem v3.8.1. *Geosci Model Dev* 2019;12:131–66. <https://doi.org/10.5194/gmd-12-131-2019>.
- [53] Sun X, Fan X, Zhang T, Wang Y, Wang Y, Lyu D, et al. Tempo-spatial distributions and transport characteristics of two dust events over northern China in March 2021. *Remote Sens* 2022;14. <https://doi.org/10.3390/rs14235967>.
- [54] Holben BN, Eck TF, Slutsker I, Tanré D, Buis JP, Setzer A, et al. AERONET—A federated instrument network and data archive for aerosol characterization. *Remote Sens Environ* 1998;66:1–16. [https://doi.org/10.1016/S0034-4257\(98\)00031-5](https://doi.org/10.1016/S0034-4257(98)00031-5).
- [55] Sinyuk A, Holben BN, Eck TF, Giles DM, Slutsker I, Korokin S, et al. The AERONET version 3 aerosol retrieval algorithm, associated uncertainties and comparisons to version 2. *Atmos Meas Tech* 2020;13:3375–411. <https://doi.org/10.5194/amt-13-3375-2020>.
- [56] Li ZQ, Xu H, Li KT, Li DH, Xie YS, Li L, et al. Comprehensive study of optical, physical, chemical, and radiative properties of total columnar atmospheric aerosols over China: An Overview of Sun–Sky Radiometer Observation Network (SONET) Measurements. *Bull Am Meteorol Soc* 2018;99:739–55. <https://doi.org/10.1175/BAMS-D-17-0133.1>.
- [57] Li L, Li Z, Li K, Blarel L, Wendisch M. A method to calculate stokes parameters and angle of polarization of skylight from polarized CIMEL sun/sky radiometers. *J Quant Spectrosc Radiat Transf* 2014;149:334–46. <https://doi.org/10.1016/j.jqsrt.2014.09.003>.
- [58] Agarwal P, Stevenson DS, Heal MR. Evaluation of WRF-Chem-simulated meteorology and aerosols over northern India during the severe pollution episode of 2016. *Atmos Chem Phys* 2024;24:2239–66. <https://doi.org/10.5194/acp-24-2239-2024>.
- [59] Carson-Marquis BN, Zhang J, Xian P, Reid JS, Marquis JW. Improving WRF-Chem meteorological analyses and forecasts over aerosol-polluted regions by incorporating NAAQS aerosol analyses. *J Appl Meteorol Climatol* 2021;60:839–55. <https://doi.org/10.1175/JAMC-D-20-0174.1>.
- [60] Cheng T, Chen H, Gu X, Yu T, Guo J, Guo H. The inter-comparison of MODIS, MISR and GOCART aerosol products against AERONET data over China. *J Quant Spectrosc Radiat Transf* 2012;113:2135–45. <https://doi.org/10.1016/j.jqsrt.2012.06.016>.
- [61] Saidou Chaibou AA, Ma X, Kumar KR, Jia H, Tang Y, Sha T. Evaluation of dust extinction and vertical profiles simulated by WRF-Chem with CALIPSO and AERONET over North Africa. *J Atmos Sol Terr Phys* 2020;199:105213. <https://doi.org/10.1016/j.jastp.2020.105213>.
- [62] Wei Y, Li Z, Zhang Y, Chen C, Dubovik O, Zhang Y, et al. Validation of POLDER GRASP aerosol optical retrieval over China using SONET observations. *J Quant Spectrosc Radiat Transf* 2020;246:106931. <https://doi.org/10.1016/j.jqsrt.2020.106931>.
- [63] Kaufman YJ, Tanré D, Remer LA, Vermote EF, Chu A, Holben BN. Operational remote sensing of tropospheric aerosol over land from EOS moderate resolution imaging spectroradiometer. *J Geophys Res Atmos* 1997;102:17051–67. <https://doi.org/10.1029/96JD03988>.
- [64] Che Y, Yu B, Parsons K, Desha C, Ramezani M. Evaluation and comparison of MERRA-2 AOD and DAOD with MODIS DeepBlue and AERONET data in Australia. *Atmos Environ* 2022;277:119054. <https://doi.org/10.1016/j.atmosenv.2022.119054>.
- [65] Zeng Y, Wang M, Zhao C, Chen S, Liu Z, Huang X, et al. WRF-Chem v3.9 simulations of the east Asian dust storm in may 2017: modeling sensitivities to dust emission and dry deposition schemes. *Geosci Model Dev* 2020;13:2125–47. <https://doi.org/10.5194/gmd-13-2125-2020>.
- [66] Dai T, Schutgens NAJ, Goto D, Shi G, Nakajima T. Improvement of aerosol optical properties modeling over eastern Asia with MODIS AOD assimilation in a global non-hydrostatic icosahedral aerosol transport model. *Environ Pollut* 2014;195:319–29. <https://doi.org/10.1016/j.envpol.2014.06.021>.
- [67] Levy R, Hsu C, et al. MODIS atmosphere L2 aerosol product. In: NASA MODIS adaptive processing system. USA: Goddard Space Flight Center; 2015. https://doi.org/10.5067/MODIS/MOD04_L2.006.
- [68] Hsu NC, Tsay S-C, King MD, Herman JR. Deep blue retrievals of Asian aerosol properties during ACE-Asia. *IEEE Trans Geosci Remote Sens* 2006;44:3180–95. <https://doi.org/10.1109/TGRS.2006.879540>.
- [69] Letu H, Ma R, Nakajima TY, Shi C, Hashimoto M, Nagao TM, et al. Surface solar radiation compositions observed from Himawari-8/9 and Fengyun-4 series. *Bull Am Meteorol Soc* 2023;104:E1772–89. <https://doi.org/10.1175/BAMS-D-22-0154.1>.
- [70] Yang S, Wang XL, Wild M. Causes of dimming and brightening in China inferred from homogenized daily clear-sky and all-sky in situ surface solar radiation records (1958–2016). *J Clim* 2019;32:5901–13. <https://doi.org/10.1175/JCLI-D-18-0666.1>.
- [71] Yang S, Wang XL, Wild M. Homogenization and trend analysis of the 1958–2016 in situ surface solar radiation records in China. *J Clim* 2018;31:4529–41. <https://doi.org/10.1175/JCLI-D-17-0891.1>.
- [72] Boylan JW, Russell AG. PM and light extinction model performance metrics, goals, and criteria for three-dimensional air quality models. *Atmos Environ* 2006;40:4946–59. <https://doi.org/10.1016/j.atmosenv.2005.09.087>.
- [73] Zhao Q, Zhao W, Bi J, Ma Z. Climatology and calibration of MERRA-2 PM2.5 components over China. *Atmos Pollut Res* 2021;12:357–66. <https://doi.org/10.1016/j.apr.2020.11.016>.
- [74] Kim K-M, Kim S-W, Choi M, Kim M, Kim J, Shin I, et al. Modeling Asian dust storms using WRF-Chem during the DRAGON-Asia field campaign in April 2012. *J Geophys Res Atmos* 2021;126:e2021JD034793. <https://doi.org/10.1029/2021JD034793>.
- [75] Tang W, Dai T, Cheng Y, Wang S, Liu Y. A study of a severe spring dust event in 2021 over East Asia with WRF-Chem and multiple platforms of observations. *Remote Sens* 2022;14:3795. <https://doi.org/10.3390/rs14153795>.
- [76] Li X, Wagner F, Peng W, Yang J, Mauzerall DL. Reduction of solar photovoltaic resources due to air pollution in China. *Proc Natl Acad Sci USA* 2017;114:11867–72. <https://doi.org/10.1073/pnas.1711462114>.
- [77] Cheng Y, Dai T, Zhang H, Xin J, Chen S, Shi G, et al. Comparison and evaluation of the simulated annual aerosol characteristics over China with two global aerosol models. *Sci Total Environ* 2021;763:143003. <https://doi.org/10.1016/j.scitotenv.2020.143003>.
- [78] Jose RS, Pérez JL, González RM, Pecci J, Palacios M. Improving air quality modelling systems by using on-line wild land fire forecasting tools coupled into WRF/Chem simulations over Europe. *Urban Clim* 2017;22:2–18. <https://doi.org/10.1016/j.uclim.2016.09.001>.
- [79] Hu Z, Huang J, Zhao C, Jin Q, Ma Y, Yang B. Modeling dust sources, transport, and radiative effects at different altitudes over the Tibetan Plateau. *Atmos Chem Phys* 2020;20:1507–29. <https://doi.org/10.5194/acp-20-1507-2020>.
- [80] Hu Z, Zhao C, Huang J, Leung LR, Qian Y, Yu H, et al. Trans-Pacific transport and evolution of aerosols: evaluation of quasi-global WRF-Chem simulation with multiple observations. *Geosci Model Dev* 2016;9:1725–46. <https://doi.org/10.5194/gmd-9-1725-2016>.